LAWRENCE
LIVERMORE
NATIONAL
LABORATORY

LLNL-JRNL-828769

Multiscale design of nonlinear materials using a Eulerian shapeoptimization scheme

A. Najafi, M. Safdari, D. A. Tortorelli, P. Geubelle

November 3, 2021

International Journal for Numerical Methods in Engineering

Disclaimer

This document was prepared as an account of work sponsored by an agency of the United States government. Neither the United States government nor Lawrence Livermore National Security, LLC, nor any of their employees makes any warranty, expressed or implied, or assumes any legal liability or responsibility for the accuracy, completeness, or usefulness of any information, apparatus, product, or process disclosed, or represents that its use would not infringe privately owned rights. Reference herein to any specific commercial product, process, or service by trade name, trademark, manufacturer, or otherwise does not necessarily constitute or imply its endorsement, recommendation, or favoring by the United States government or Lawrence Livermore National Security, LLC. The views and opinions of authors expressed herein do not necessarily state or reflect those of the United States government or Lawrence Livermore National Security, LLC, and shall not be used for advertising or product endorsement purposes.

IM release number LLNL-JRNL-828769

Multiscale design of nonlinear materials using a Eulerian shape optimization scheme

Ahmad R. Najafi[1*], Masoud Safdari[2], Daniel A. Tortorelli[3,4], Philippe H. Geubelle[2]

[1]*Department of Mechanical Engineering and Mechanics, Drexel University, Philadelphia, PA 19104, USA*

[2]*Department of Aerospace Engineering, University of Illinois, Urbana, Illinois, IL 61801, USA*

[3]*Department of Mechanical Science and Engineering, University of Illinois, Urbana, Illinois, IL 61801, USA*

[4]*Director, Center for Design and Optimization, Lawrence Livermore National Laboratory Livermore, CA, USA*

SUMMARY

Motivated by recent advances in manufacturing, the design of materials is in the focal point of interest in the material research community. One of the critical challenges in this field is finding optimal material microstructure for a desired macroscopic response. This work presents a computational method for mesoscale-level design of particulate composites for an optimal macroscale-level response. The method relies on a custom shape optimization scheme to find the extrema of a nonlinear cost function subject to a set of constraints. Three key 'modules' constitute the method: multiscale modeling, sensitivity analysis, and optimization. Multiscale modeling relies on a classical homogenization method and a non-linear NURBS-based generalized finite element scheme to efficiently and accurately compute the structural response of particulate composites using a non-conformal discretization. A three-parameter isotropic damage law is used to model microstructure-level failure. An analytical sensitivity method is developed to compute the derivatives of the cost/constraint functions with respect to the design variables that control the microstructure's geometry. The derivation uncovers subtle but essential new terms contributing to the sensitivity of finite element shape functions and their spatial derivatives. Several structural problems are solved to demonstrate the applicability, performance, and accuracy of the method for the design of particulate composites with a desired macroscopic nonlinear stress-strain response.

Received . . .

(2020)

2020; **00**:2–57
KEY WORDS: Gradient-based shape optimization; NURBS; Nonlinear GFEM; Fixed grid; Analytical sensitivity analysis

1. INTRODUCTION

The precise evaluation of the effective properties of heterogeneous materials has a long and rich history, attracting researchers from multiple disciplines. Various theoretical [1–3] and computational [4–6] micromechanics approaches have been widely used to characterize the structure-property relationships of heterogeneous material systems. The primary objective of these studies is to find the effective properties of a heterogeneous material for a given set of the phase properties and microstructure. However, over the last two decades, many researchers restated this question as an inverse problem, i.e., how can the different phases of a heterogeneous material be distributed to target or optimize a particular macroscopic material property [7].

The aforementioned inverse problem is an optimization problem and has been solved via different optimization techniques. Among these different approaches, topology optimization is the most popular wherein it is combined with homogenization tools to develop the so-called inverse homogenization approach. For example, Sigmund [8, 9] used it to optimize the microstructure of a periodic unit cell for minimum weight with prescribed macroscopic elastic and thermoelastic properties. It has since been employed to design composite materials with extreme elastic or thermal expansion [10–13], fluid transport [14], auxetic [15–18], and other multifunctional [19–21] properties. Osanov and Guest [22] provides a good review of this topic.

Even though topology optimization approaches have been mostly employed for the design of structures with the linear elastic response, some topology optimization studies considered material and geometrical nonlinearities for structural design applications. Some researchers have addressed geometrical nonlinearity in topology optimization. These include Jog [23], Buhl et. al. [24], Bruns and co-authors [25–28], Kwak and Cho [29], Abdi et al. [30], Chen et al. [31], Deng [32],

*Correspondence to: Department of Mechanical Engineering and Mechanics, Drexel University, Philadelphia, PA 19104, USA, Phone: (215) 571-4578, Fax: (215) 895 1478, Email: arn55@drexel.edu

Dunning [33], Xu et al. [34], and Zhu et al. [35]. Other authors have investigated the topology optimization of nonlinear structures [36–49]. Yuge and Kikuchi [36], Maute et al. [38], Yoon and Kim [39], Alberdi et al. [47], and Zhao et al. [49] have used topology optimization to design structures undergoing plastic deformation. Several authors have also incorporated damage materials models into the topology design of continuum structures [37, 41–43, 45]. More recently, advances in high-performance computing have set the stage for the computationally intensive design of nonlinear structures based on multiscale topology optimization [50–55].

Topology optimization has also been combined with nonlinear homogenization for the design of material microstructure to achieve prescribed macroscopic properties. For example, Swan in collaboration with Arora [56] and Kosaka [57] has studied the topological design of elastic and inelastic composite materials. Some other authors used this approach to design auxetic metamaterials [55, 58–62] and cellular materials [46] with prescribed nonlinear properties.

In contrast to the abundant studies on inverse homogenization using topology optimization, limited studies have been devoted to combining shape optimization and inverse homogenization for the design of composite materials. In one of a very few related studies, Ibrahimbegovic et al. [63] investigated the shape optimization of a two-phase inelastic composite microstructure, in which the matrix phase exhibited plasticity and the inclusion phase damage. The interface geometry in a periodic cell containing a single inclusion was optimized to maximize the amount of plastic dissipation or the external work. Other authors combined a 2D isogeometric shape optimization and inverse linear homogenization to design periodic microstructures [64] and auxetic materials [65, 66]. In a recent publication [67], some of the authors of the present manuscript developed a multiscale shape optimization scheme to design the microstructure of 3D particulate composites to obtain a desired nonlinear response. In that study, the framework was built on an Interface-enriched Generalized Finite Element Method (IGFEM) [68–70] and the material nonlinearities were associated with interfacial debonding of inclusions from a surrounding matrix, which was modeled using a cohesive failure model.

Herein, we develop and implement a shape optimization method to design composite material microstructures based on a NURBS-based Interface-enriched Generalized Finite Element Method (NIGFEM) to achieve a prescribed macroscopic behavior. This work builds on our previous studies ([71] and [72]) that introduced two Eulerian-based shape optimization schemes by incorporating the IGFEM [68–70,73] and NIGFEM [74–77], respectively. Similar studies are performed to design microvascular panels for active cooling applications [78–85].

The composite material design problem is illustrated in Figure 1. The design domain is a periodic unit cell consisting of several inclusions. Its homogenized macroscopic nonlinear behavior is denoted by the solid black curve in Figure 1(b). The optimization goal is to find the geometry and material properties of the inclusions to achieve the desired macroscopic response, depicted by the dashed red line in the same figure, in other words the goal is to minimize the shaded area between the two curves.

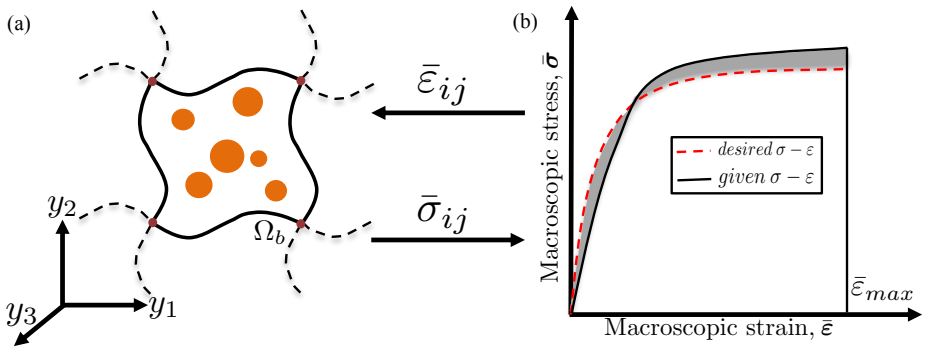

Figure 1. (a) Schematic of a deformed periodic unit cell; (b) unit cell and desired macroscopic stress-strain curves. The optimization finds the desired microstructure to minimize the shaded area between the two curves.

We formulate this problem as an inverse homogenization problem that is solved via shape optimization. The desired nonlinear macroscopic structural response is attributed to the multi-phase composite material that is modeled with irreversible isotropic damage laws. To perform the sensitivity analysis for this optimization problem, we derive an analytic direct differentiation sensitivity formulation in the NIGFEM framework. Combining shape optimization, NIGFEM, and computational homogenization, we develop a design framework to optimize the microstructure of a composite material to attain a prescribed macroscopic nonlinear behavior. In contrast to our previous

study on the multiscale nonlinear design of 3D particulate composites [67], we use a continuum damage law to introduce the material nonlinearities to our models. Here, we adopt a NURBS-based IGFEM that provides a more accurate description of the geometry and stress-strain modeling over a relatively coarse mesh.

The organization of this paper is as follows. In the next section, the construction of the NIGFEM enrichment functions for 3D problems is summarized. Section 3 is devoted to the computational homogenization of general linear/nonlinear elastic periodic composites. We then discuss the damage model in Section 4 and describe the numerical algorithm used to simulate the evolution of damage. In Section 5, the optimization problem and sensitivity analysis are described. Numerical verification and application examples are presented in Sections 6 and 7, respectively.

2. 3D NIGFEM ENRICHMENT FUNCTIONS

The NIGFEM formulation for 2D problems has been presented in [72, 74, 86], while the 3D NIGFEM implementation appears in [75]. To avoid repetition, a summary of the key concepts and notations associated with the NURBS and NIGFEM formulations are presented in Appendices A and B, respectively, and only the construction of the 3D NIGFEM enrichment functions is described in this section.

To introduce 3D NIGFEM enrichment functions, let us consider a structural problem on a heterogenous domain. We discretize the domain $\Omega \cong \Omega^h$ with a fixed mesh that conforms to the fixed domain boundary $\partial\Omega$ but not to the material interfaces Γ_i, cf. Figure 2. The displacement field in each element intersected by the interface Γ_i is approximated as

$$\mathbf{u}^h(\mathbf{y}) = \sum_{i=1}^{n_e} N_i(\mathbf{y})\mathbf{u}_i + \sum_{j=1}^{n_{\psi_j}} \sum_{k=1}^{n_{\psi_k}} \psi_{jk}(\mathbf{y})\boldsymbol{\alpha}_{jk}. \tag{1}$$

The first sum on the right-hand side of (1) represents the classical finite element interpolation with n_e standard Lagrangian shape functions, $N_i(\mathbf{y})$, and the standard nodal dofs $\mathbf{u}_i = [u_i^{y_1}\ u_i^{y_2}\ u_i^{y_3}]^T$. The second sum represents the augmented contribution with the $n_\psi = n_{\psi_j} \times n_{\psi_k}$ enrichment functions

$\psi_{jk}(\mathbf{y})$ and their associated generalized dofs $\boldsymbol{\alpha}_{jk} = \left[\alpha_{jk}^{y_1}\ \alpha_{jk}^{y_2}\ \alpha_{jk}^{y_3}\right]^T$, where n_{ψ_j} and n_{ψ_k} are the number of enrichment functions along the two parametric directions that define the NURBS surface that models the material interface Γ_i within the element. The number of NURBS basis functions, n_ψ, depends on the level of geometric complexity of the material interfaces and the discretization of the underlying mesh [74, 75].

To construct the enrichment functions for the NIGFEM, consider the domain Ω^h, shown in Figure 2(a), discretized by a non-conforming structured mesh composed of n_e standard trilinear hexahedral elements Ω_i^h. The domain Ω^h contains a material interface Γ represented by a NURBS surface[†] of order p and q such that

$$\Gamma = \left\{ (\xi,\, \eta) \in [0,1] \times [0,1] : \mathbf{y} = \boldsymbol{S}(\xi,\, \eta) = \sum_{i=1}^{l}\sum_{j=1}^{m} R_{i.j,p.q}(\xi,\, \eta)\, \mathbf{P}_{i.j} \right\}, \tag{2}$$

where $R_{i.j,p.q}(\xi,\, \eta)$ are the rational B-spline basis functions, i.e., the NURBS basis functions, defined in (A.8), $\{\mathbf{P}_{i.j}\}$ ($i = 1,\, 2,\, ...,\, l,\ j = 1,\, 2,\, ...,\, m$) is an array of control points that define the net, and (ξ,η) is the pair of parametric surface coordinates (knot vectors), all introduced in Appendix A. We assume without loss of generality that the material interface is a straight cylindrical inclusion normal to a plane of the non-conforming mesh shown in Figure 2(a)[‡]. As illustrated in Figure 2(b), we consider two possible arrangements for a hexahedral element that is split by a straight cylindrical inclusion. To generate enrichment functions for such an element Ω_e, we need to construct 3D NURBS volumes of the element subdomains $\Omega_e^{(1)}$ and $\Omega_e^{(2)}$, as shown in Figure 2(d). This is a three-step process. We first intersect the material interface Γ with the element faces $\partial\Omega_e$ and use the global intersection calculation procedure introduced in [87] to find four boundary NURBS curves $\boldsymbol{C}_i^{e}$[§], $i = 1, \ldots, 4$, as shown in Figure 2(c). In the second step, we define a portion of the material interface Γ_e residing in the element Ω_e. In general, Γ_e is not a NURBS surface. Therefore, we need to find a NURBS approximation to Γ_e, which we refer to as Γ_e^h in Figure 2(c). To construct

[†] Without loss of generality, we assume that the material interface Γ is represented by a bi-quadratic NURBS surface $\boldsymbol{S}(\xi,\, \eta)$.

[‡] For more complex geometric combinations arising from the intersection of a material interface Γ_e with a hexahedral element Ω_e, we refer to [75].

[§] Since Γ is a bi-quadratic surface in this study, the $\boldsymbol{C}_i^e$ are at least quadratic.

Γ_e^h, we generate a bilinearly blended Coons surface [87] from the boundary of Γ_e, i.e., from the four NURBS curves $\boldsymbol{C}_i^e$, $i = 1, \ldots, 4$ (Figure 2(c)). Γ_e^h is referred to hereafter as the sub-interface and it is worth mentioning that the order of the Coons surface is dictated by the order of boundary NURBS curves $\boldsymbol{C}_i^e$¶. Finally, the element boundaries $\partial\Omega_e$ and interface Γ_e^h are used to construct the 3D NURBS volumes for the subdomains $\Omega_e^{(1)}$ and $\Omega_e^{(2)}$, cf. Figure 2(d). These volumes are used to define the enrichment functions ψ_{jk} of (1). We repeat this three-step procedure for every element Ω_e intersected by Γ.

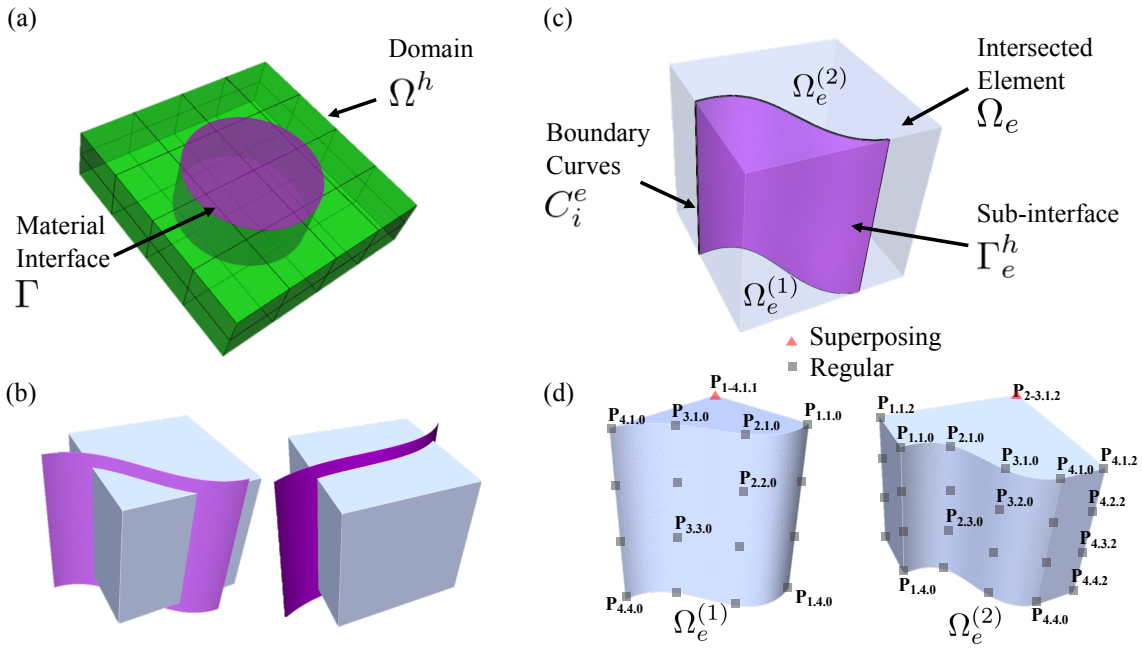

Figure 2. (a) NIGFEM domain with a cylindrical interface $\boldsymbol{S}(\xi, \eta)$ discretized by a non-conforming structured mesh of trilinear hexahedral elements; (b) two possible geometric configurations for elements traversed by straight cylindrical material interface; (c-d) Reconstruction of NURBS surface $\boldsymbol{\Gamma}_e^h$ from the computed boundary curves C_i^e and NURBS volume $\boldsymbol{\Omega}_i^e, i = 1, 2$ corresponding to the intersected element.

For more clarification, let us further explain the procedure of constructing the NURBS representation of the subdomain $\Omega_e^{(i)}$ $(i = 1, 2)$. As seen in Figure 2(d), the element Ω_e is divided into two curvilinear subdomains $\Omega_e^{(1)}$ and $\Omega_e^{(2)}$ that meet at the internal interface Γ_e^h . These subdomains $\Omega_e^{(1)}$ and $\Omega_e^{(2)}$ are the integration elements. To build 3D NURBS volumes for these integration elements, we choose the order of the basis functions for $\Omega_e^{(i)}$ to be $p = q = 2$ in the

¶The quadratic boundary curves $\boldsymbol{C}_i^e$ ensure the Coons surface of Γ_e^h is bi-quadratic NURBS surface.

ξ- and η-directions[‖], along the interface, and $r = 1$ in the ζ-direction that is perpendicular to the interface. We also use $m = n = 4$ control points in the parametric ξ- and η-directions, and two in the ζ-direction[**]. To reproduce the edges of $\Omega_e^{(i)}$, we use superposing control points. As illustrated in Figure 2(d), sixteen control points $\{\mathbf{P}_{j.k.0}\}$ ($j, k = 1, ..., m = n = 4$) define the sub-interface Γ_e^h of $\Omega_e^{(1)}$ (See Appendix C for details on how we define these control points). We subsequently introduce sixteen dummy[††] control points $\{\mathbf{P}_{j.k.1}\}$ ($j, k = 1, ..., m = n = 4$), i.e., four-four times control points superimposed to model the element edges. The 4-times superposed control points $\{\mathbf{P}_{1-4,1,1}\}$ and $\{\mathbf{P}_{1-4,4,1}\}$ are coincident with two nodes of the element Ω_e^1, and the 4-times superimposed control points $\{\mathbf{P}_{1-4.k.1}\}$ ($k = 2, 3$) are uniformly spaced between them. We then define a knot vector for each parametric direction based on the order of the subdomains and the number of control points in their directions. We use normalized knot vectors $\boldsymbol{\Xi} = \boldsymbol{\mathcal{H}} = \{0, 0, 0, 0.5, 1, 1, 1\}$ for the parametric ξ- and η-directions, and $\boldsymbol{\mathcal{Z}} = \{0, 0, 1, 1\}$ for the ζ-direction. Using the control net $\{\mathbf{P}_{j.k.l}\}$, $j, k = 1, ..., 4$, $l = 0, 1$ and knot vectors $\boldsymbol{\Xi}, \boldsymbol{\mathcal{H}}$, and $\boldsymbol{\mathcal{Z}}$, we build the 3D NURBS volume for subdomain $\Omega_e^{(1)}$. The same approach is employed to construct a NURBS volume for the integration element $\Omega_e^{(2)}$, utilizing $\{\mathbf{P}_{j.k.l}\}$ ($j, k = 1, ..., 4$, $l = 0, 2$) and the same knot vectors $\boldsymbol{\Xi}, \boldsymbol{\mathcal{H}}$, and $\boldsymbol{\mathcal{Z}}$. The NURBS basis functions associated with the integration elements $\Omega_e^{(1)}$ and $\Omega_e^{(2)}$ are denoted by $R^{(1)}_{j.k.l,p.q.r}$ and $R^{(2)}_{j.k.l,p.q.r}$, with $l = 0, 1$ for $\Omega_e^{(1)}$, $l = 0, 2$ for $\Omega_e^{(2)}$, and $j, k = 1, ..., 4$ as shown in Figure 2(d). Since we have assumed $p = q = 2$ and $r = 1$ in this study, we hereafter drop the subscripts p, q, and r from the NURBS basis for convenience.

The enrichment functions $\psi_{jk}(\mathbf{y})$ correspond to the control points $\{\mathbf{P}_{j.k.0}\}$ along the material interface and are defined piecewise as

$$\psi_{jk}(\mathbf{y}) = \begin{cases} \psi^{(1)}_{jk}(\mathbf{y}) = R^{(1)}_{j.k.0}(\mathbf{y}) \ \text{ if } \mathbf{y} \in \Omega_e^{(1)} \\ \psi^{(2)}_{jk}(\mathbf{y}) = R^{(2)}_{j.k.0}(\mathbf{y}) \ \text{ if } \mathbf{y} \in \Omega_e^{(2)} \end{cases} \qquad j, k = 1, \ ..., \ 4 \ . \tag{3}$$

[‖] The order of the approximation for the basis functions is arbitrary in the NIGFEM, and, for a highly curvilinear interface, we may improve the precision of the approximation by choosing higher-order basis functions.

[**] The number of control points in each parametric direction can vary depending on the geometric complexity of Γ_e.

[††] These control points are called 'dummy' because no degree-of-freedom is associated with them. They are solely used to construct NURBS volumes.

The enrichment functions $\psi_{jk}(\mathbf{y})$ are non-zero only in the interior of Ω_e, i.e., they vanish on the faces of Ω_e that do not intersect the interface Γ_e. Moreover, these functions are C^0-continuous in Ω_e. Therefore, the displacement field $\mathbf{u}^h$ is also C^0-continuous.

3. COMPUTATIONAL HOMOGENIZATION

The objective of homogenization techniques is to determine the effective overall (macroscopic) properties of a heterogeneous material. They have been developed for linear and nonlinear materials in [88–90]. In this study, we adopt the homogenization scheme described in [89], where it is assumed that the macroscopic structure is formed by a repeating composite unit cell, where the size of the unit cell is very small compared to the macroscopic structure.

To begin, let us consider a macroscopic body, Ω_M, wherein each point $X \in \Omega_M$ is assigned a representative volume element, i.e., unit cell, which models the heterogeneous microstructure. In our study we assume each volume element is identical, i.e., we use periodic unit cells $\Omega_b = \frac{\epsilon}{2}[-1,\,1]^3$, where ϵ is microstructure length scale. We also assume there are no instability or bifurcation phenomena at the microstructural scale that break the symmetry of the periodic unit cell resulting in the non-convexity of the microscopic strain energy density function. Assuming that the microstructural length scale is much smaller than its macroscopic counterpart, we decompose the displacement solution in Ω_b as

$$\mathbf{u}(\mathbf{y}) = \nabla\bar{\mathbf{u}}\mathbf{y} + \tilde{\mathbf{u}}(\mathbf{y}), \tag{4}$$

where $\tilde{\mathbf{u}}$ is the perturbation (i.e., fluctuating) displacement due to the material heterogeneities (that is periodic and has zero average on Ω_b), $\bar{\mathbf{u}}$ denotes the macroscopic displacement gradient, and $\mathbf{y}$ is a point coordinate in Ω_b. Owing to the assumption of periodicity, all admissible displacements fields $\mathbf{u} \in \mathcal{V}$ where

$$\mathcal{V} = \left\{\mathbf{v} \middle|\, \mathbf{v} \in H^1(\Omega_b)\,;\, \mathbf{v} = \mathbf{A}\mathbf{y} + \tilde{\mathbf{v}}\right\}, \tag{5}$$

in which H^1 is a Hilbert space, $\mathbf{A}$ is an arbitrary real second-order tensor, and $\tilde{\mathbf{u}} \in \tilde{\mathcal{V}}$ where

$$\tilde{\mathcal{V}} = \left\{ \tilde{\mathbf{v}} \middle| \, \tilde{\mathbf{v}} \in H^1(\Omega_b) \, ; \, \tilde{\mathbf{v}} \text{ has zero average and is Y-periodic on } \partial\Omega_b \right\}. \tag{6}$$

The local strain in Ω_b with the small strain assumption takes the form

$$\boldsymbol{\varepsilon}(\mathbf{y}) = \bar{\boldsymbol{\varepsilon}} + \tilde{\boldsymbol{\varepsilon}}(\mathbf{y}), \tag{7}$$

where $\bar{\boldsymbol{\varepsilon}} = \frac{1}{2}\left(\nabla\bar{\mathbf{u}} + (\nabla\bar{\mathbf{u}})^T\right)$ is the macroscopic strain and

$$\tilde{\boldsymbol{\varepsilon}} = \frac{1}{2}\left(\nabla\tilde{\mathbf{u}} + (\nabla\tilde{\mathbf{u}})^T\right). \tag{8}$$

is the perturbation strain.

In our strain-controlled homogenization problem, we impose a history of macroscopic strain $\bar{\boldsymbol{\varepsilon}}$ on the unit cell and compute the corresponding perturbation displacement field $\tilde{\mathbf{u}}$ by enforcing equilibrium [56]. The periodicity of $\tilde{\mathbf{u}}$ leads to the periodicity of $\nabla\tilde{\mathbf{u}}$. And assuming strains and stresses are linear on the boundary of the unit cell, it can be shown that the traction $\boldsymbol{\sigma}_n = \boldsymbol{\sigma} \cdot \mathbf{n}$ is aperiodic [56] and thus, equilibrium, in the absence of body forces, requires that $\mathbf{u} \in \mathcal{V}$ satisfies

$$\int_{\Omega_b} \boldsymbol{\sigma}(\mathbf{u}) : \boldsymbol{\varepsilon}(\delta\tilde{\mathbf{u}}) \, d\Omega = 0, \tag{9}$$

for all $\tilde{\mathbf{u}} \in \tilde{\mathcal{V}}$.

Having $\boldsymbol{\sigma}$ from (9), we compute the homogenized macroscopic stress $\bar{\boldsymbol{\sigma}}$ as [56, 89]

$$\bar{\boldsymbol{\sigma}} = \frac{1}{|\Omega_b|}\int_{\Omega_b} \boldsymbol{\sigma} d\Omega. \tag{10}$$

Marching through time, we evaluate the response trajectory by computing the perturbation displacement field $\tilde{\mathbf{u}}$ from (9) and then the corresponding macroscopic stress $\bar{\boldsymbol{\sigma}}$ from (10).

4. DAMAGE MECHANICS

To introduce nonlinearity to our model, we adopt the irreversible isotropic damage law suggested by [91, 92]. In this section, we first summarize the model. Then, we outline our numerical implementation and highlight important aspects of the coupled nonlinear analysis.

4.1. *Isotropic continuum damage model*

The damage model is based on the following form of the free energy potential [91]:

$$\psi\left(\boldsymbol{\varepsilon},\omega\right)=\left(1-\omega\right)\psi_0\left(\boldsymbol{\varepsilon}\right), \tag{11}$$

where $\psi_0\left(\boldsymbol{\varepsilon}\right)$[‡‡] is the initial elastic stored energy function in an undamaged (virgin) material, given for the linear case by

$$\psi_0\left(\boldsymbol{\varepsilon}\right)=\frac{1}{2}\boldsymbol{\varepsilon}:\mathbf{D}_0:\boldsymbol{\varepsilon}, \tag{12}$$

where $\mathbf{D}_0$ is the positive definite linear isotropic elasticity tensor. The factor $(1-\omega)$ on the right-hand side of (11) provides the coupling between elasticity and damage.

Using the constitutive assumption (11) and the Clausius−Duhem inequality

$$-\dot{\psi}+\boldsymbol{\sigma}:\dot{\boldsymbol{\varepsilon}}\geq 0. \tag{13}$$

It can be shown that the stress tensor satisfies

$$\boldsymbol{\sigma}=\frac{\partial\psi\left(\boldsymbol{\varepsilon},\omega\right)}{\partial\boldsymbol{\varepsilon}}=\left(1-\omega\right)\frac{\partial\psi_0\left(\boldsymbol{\varepsilon}\right)}{\partial\boldsymbol{\varepsilon}}, \tag{14}$$

a thermodynamic force Y exist such that

$$Y=\frac{\partial\psi\left(\boldsymbol{\varepsilon},\omega\right)}{\partial\omega}=-\psi_0\left(\boldsymbol{\varepsilon}\right), \tag{15}$$

[‡‡] We assume that $\boldsymbol{\varepsilon}\rightarrow\psi_0\left(\boldsymbol{\varepsilon}\right)$ is a convex function.

and dissipation inequality is defined as

$$\mathcal{D} = -Y\dot{\omega} \geq 0. \tag{16}$$

In the above, $-Y$ is called the "damage strain energy release rate" and, since $-Y$ is non-negative, we can interpret from (16) that $\dot{\omega} \geq 0$, i.e., the damage is not reversible.

Analogous to the yield surface in plasticity theory, we assume that damage occurs if the following damage condition is violated,

$$g\left(Y\right) = G\left(-Y\right) - \omega \leq 0, \tag{17}$$

where everything is a function of time and at time $t = 0$, $\omega(t) = \omega^0 = 0$. In (17), the progressive degradation of the mechanical properties due to damage is characterized by the function G, which is represented by a three-parameter Weibull distribution [93],

$$G\left(Y\right) = 1 - exp\left[-\left(\frac{Y - Y_{in}}{p_1 Y_{in}}\right)^{p_2}\right], \tag{18}$$

where Y_{in} is the initial threshold, and p_1, and p_2 define the dimensional scale, and shape of the curve. The isotropic damage model (18) is able to represent a wide range of materials.

To capture the damage growth, we minimize the regularized dissipation function

$$\mathcal{D}_\mu = -\mathcal{D} + \frac{1}{2}\mu\left\langle\phi\left(g\right)\right\rangle^2, \tag{19}$$

where μ is the damage fluidity coefficient, the scalar valued function ϕ is the viscous damage flow function, and the symbol $\langle\rangle$ denotes McAuley brackets. In the current study, we assume linear viscous damage, i.e., $\phi\left(g\right) \equiv g$, as suggested in [91, 92]. We then solve

$$\min_Y \mathcal{D}_\mu = -\mathcal{D} + \frac{1}{2}\mu\left\langle g\right\rangle^2 = Y\dot{\omega} + \frac{1}{2}\mu\left\langle g\right\rangle^2, \tag{20}$$

and the Karush-Kuhn-Tucker optimality conditions require

$$\dot{\omega} = -\mu \langle g \rangle \frac{\partial g}{\partial Y}. \tag{21}$$

Expanding the right-hand side of (21) gives

$$\dot{\omega} = \mu \langle g \rangle G'(-Y), \tag{22}$$

By excluding the $G'(-Y) > 0$ contribution in (22) as suggested in [94], the evolution of ω is reduced to

$$\dot{\omega} = \mu \langle g \rangle . \tag{23}$$

The damage model described above is the rate-dependent (viscous) damage model presented in [91, 92] by introducing the damage fluidity coefficient μ. This model addresses the issues associated with rate-independent models that may lead to loss of strong material ellipticity, which manifests itself with localization phenomenon and mesh-sensitivity numerical computations. As μ approaches zero, the model exhibits instantaneous elastic behavior, whereas, for μ approaching infinity, the model exhibits rate-independent behavior.

4.2. Coupled nonlinear analysis

The analysis of a coupled damage-elasticity problem with nonlinear history-dependent material response can be performed by applying the algorithm for transient nonlinear coupled systems described in [95]. Let $\mathbb{U}$, $\mathbb{W}$, $\mathbb{R}$, and $\mathbb{H}$ denote the displacement, damage state variables, equilibrium residual, and damage evolution residual vectors. A transient nonlinear coupled system at time ${}^{n}t$ can be expressed in residual form as

$$\begin{aligned} {}^{n}\mathbb{R}\left({}^{n}\mathbb{U}, {}^{n-1}\mathbb{U}, {}^{n}\mathbb{W}, {}^{n-1}\mathbb{W}\right) &= \mathbf{0}, \\ {}^{n}\mathbb{H}\left({}^{n}\mathbb{U}, {}^{n-1}\mathbb{U}, {}^{n}\mathbb{W}, {}^{n-1}\mathbb{W}\right) &= \mathbf{0}, \end{aligned} \tag{24}$$

where ${}^{n}\mathbb{R}$ and ${}^{n}\mathbb{H}$ are global equilibrium and local damage evolution residuals at time step ${}^{n}t$, ${}^{n}\mathbb{U}$ and ${}^{n-1}\mathbb{U}$ are the global displacement response vectors and ${}^{n}\mathbb{W}$ and ${}^{n-1}\mathbb{W}$ are the local damage

state variables at time steps ${}^{n}t$ and ${}^{n-1}t$. Suppressing ${}^{n-1}t$ terms known quantities, (24) is written as

$$\begin{aligned} {}^{n}\mathbb{R}\left({}^{n}\mathbb{U},{}^{n}\mathbb{W}\right)&=\mathbf{0},\\ {}^{n}\mathbb{H}\left({}^{n}\mathbb{U},{}^{n}\mathbb{W}\right)&=\mathbf{0}. \end{aligned} \tag{25}$$

As usual for nonlinear problems, the coupled nonlinear system (25) can be solved iteratively by implementing the Newton-Raphson method to obtain ${}^{n}\mathbb{U}$ and ${}^{n}\mathbb{W}$ wherein ${}^{n}\mathbb{R}$ and ${}^{n}\mathbb{H}$ are assembled into a single residual as

$${}^{n}\mathcal{R}\left({}^{n}\mathcal{U}\right)=\begin{bmatrix} {}^{n}\mathbb{R}\left({}^{n}\mathbb{U},{}^{n}\mathbb{W}\right)\\ {}^{n}\mathbb{H}\left({}^{n}\mathbb{U},{}^{n}\mathbb{W}\right) \end{bmatrix}=0, \tag{26}$$

where

$${}^{n}\mathcal{U}=\begin{bmatrix} {}^{n}\mathbb{U}\\ {}^{n}\mathbb{W} \end{bmatrix}. \tag{27}$$

However, following [96], another way to obtain the solution of this coupled problem is to uncouple it by treating the local response $\mathbb{W}$ as a function of the global response $\mathbb{U}$ and implementing the Schur component Newton-Raphson scheme in two nested iterative loops, as described in [95,97]. In this approach, (25) is written as

$$\begin{aligned} {}^{n}\mathbb{R}\left({}^{n}\mathbb{U},{}^{n}\mathbb{W}\left({}^{n}\mathbb{U}\right)\right)&=\mathbf{0},\\ {}^{n}\mathbb{H}\left({}^{n}\mathbb{U},{}^{n}\mathbb{W}\left({}^{n}\mathbb{U}\right)\right)&=\mathbf{0}. \end{aligned} \tag{28}$$

First, we evaluate the local response ${}^{n}\mathbb{W}\left({}^{n}\mathbb{U}\right)$ in the inner loop by solving the local residual of (28) using the Newton-Raphson method for a fixed ${}^{n}\mathbb{U}$. In this iteration, the incremental response $\delta\mathbb{W}$ is computed as

$$\frac{\partial^{n}\mathbb{H}}{\partial^{n}\mathbb{W}}\left({}^{n}\mathbb{U},{}^{n}\mathbb{W}^{J}\left({}^{n}\mathbb{U}\right)\right)\delta\mathbb{W}=-{}^{n}\mathbb{H}\left({}^{n}\mathbb{U},{}^{n}\mathbb{W}^{J}\left({}^{n}\mathbb{U}\right)\right), \tag{29}$$

where $\dfrac{\partial\mathbb{H}}{\partial\mathbb{W}}$ is called the local tangent operator. Computing the incremental response $\delta\mathbb{W}$, the local response is updated as

$${}^{n}\mathbb{W}^{J+1}\left({}^{n}\mathbb{U}\right)={}^{n}\mathbb{W}^{J}\left({}^{n}\mathbb{U}\right)+\delta\mathbb{W}. \tag{30}$$

We repeat the Newton-Raphson subiterations in the inner loop until it converges to obtain ${}^{n}\mathbb{W}\left({}^{n}\mathbb{U}\right)$.

Linearizing the global residual equation in (28) and implementing the Newton-Raphson method in the outer loop results in the following equation for the incremental response $\delta\mathbb{U}$:

$$\begin{aligned}&\left[\frac{\partial^{n}\mathbb{R}}{\partial^{n}\mathbb{U}}\left({}^{n}\mathbb{U}^{I},{}^{n}\mathbb{W}\left({}^{n}\mathbb{U}^{I}\right)\right)+\right.\\&\left.\frac{\partial^{n}\mathbb{R}}{\partial^{n}\mathbb{W}}\left({}^{n}\mathbb{U}^{I},{}^{n}\mathbb{W}\left({}^{n}\mathbb{U}^{I}\right)\right)\frac{\partial\mathbb{W}}{\partial\mathbb{U}}\left({}^{n}\mathbb{U}^{I}\right)\right]\delta\mathbb{U}=-{}^{n}\mathbb{R}\left({}^{n}\mathbb{U}^{I},{}^{n}\mathbb{W}\left({}^{n}\mathbb{U}^{I}\right)\right),\end{aligned}\tag{31}$$

where the term in square brackets represents the global tangent operator and

$$\frac{\partial\mathbb{W}}{\partial\mathbb{U}}\left({}^{n}\mathbb{U}^{I}\right)=-\left(\frac{\partial^{n}\mathbb{H}}{\partial^{n}\mathbb{W}}\left({}^{n}\mathbb{U}^{I},{}^{n}\mathbb{W}\left({}^{n}\mathbb{U}^{I}\right)\right)\right)^{-1}\frac{\partial^{n}\mathbb{H}}{\partial^{n}\mathbb{U}}\left({}^{n}\mathbb{U}^{I},{}^{n}\mathbb{W}\left({}^{n}\mathbb{U}^{I}\right)\right),\tag{32}$$

240 follows from differentiating the local residual equation $\mathbb{H}=0$. Upon evaluating the incremental response $\delta\mathbb{U}$, the global response in the next iteration, ${}^{n}\mathbb{U}^{I+1}$, is obtained from

$${}^{n}\mathbb{U}^{I+1}={}^{n}\mathbb{U}^{I}+\delta\mathbb{U}.\tag{33}$$

The iteration-subiteration process in two nested Newton-Raphson loops is repeated for each iterate ${}^{n}\mathbb{U}^{I}$ until the global residual equation (28) converges.

In a multiscale NIGFEM framework, the elastic-damage coupled nonlinear problem presented in
245 Section (4.1) is solved by the local-global algorithm described above. Combining the weak form (9) and the finite element discretization provides equilibrium residual vector,

$$\mathbb{R}\left({}^{n}\tilde{\mathbf{U}}^{e},{}^{n}\omega\right)=\underset{e}{\mathbb{A}}\int_{\Omega_{e}}\mathbb{B}^{T}\boldsymbol{\sigma}\left({}^{n}\tilde{\mathbf{U}}^{e},{}^{n}\omega\right)d\Omega_{e}=\underset{e}{\mathbb{A}}\sum_{\text{Gauss points}}\mathbb{B}^{T}{}^{n}\boldsymbol{\sigma}\,w\,|\mathbf{J}|=\underset{e}{\mathbb{A}}\sum_{\text{Gauss points}}{}^{n}\mathbf{R}_{gp},\tag{34}$$

where $\underset{e}{\mathbb{A}}$ is the finite element assembly operator, Ω_{e} is the finite element domain ($\Omega_{b}\cong\bigcup_{e=1}^{N_{e}}\Omega_{e}$ for N_{e} finite elements), $\mathbb{B}$ is the strain displacement matrix defined in Appendix B, ${}^{n}\tilde{\mathbf{U}}^{e}$ is the vector of nodal element perturbation displacements (cf. (4)), and ${}^{n}\omega$ is the vector of Gauss point damage
250 state variables. As seen above the integral is approximated via a Gaussian quadrature where $\mathbf{J}$ is the Jacobian of the isoparametric mapping, w is the Gauss weight, and ${}^{n}\boldsymbol{\sigma}$ is the stress tensor defined

by (12) and (14),

$$ {}^{n}\boldsymbol{\sigma} = (1 - {}^{n}\omega)\, \mathbf{D}_0 \left(\bar{\boldsymbol{\varepsilon}} + \mathbb{B}^{n}\tilde{\mathbf{U}}^{e} \right), \tag{35} $$

where $\bar{\boldsymbol{\varepsilon}}$ is the macroscopic strain introduced in (7). Finally, ${}^{n}\mathbf{R}_{gp}$ is ellement guass point residual.

Before evaluating ${}^{n}\mathbf{R}_{gp}$ in (34), one needs to compute the Gauss point damage variables ${}^{n}\omega$ by resolving the local residual equations. If the damage criterion (17) is violated or if $g = 0$, the local residual equation is formed from the damage evolution Equation (23) and the implicit backward Euler scheme as:

$$ {}^{n}H_{gp}\left({}^{n}\tilde{\mathbf{U}}^{e},\, {}^{n}\omega \right) = \frac{\left({}^{n-1}\omega + \Delta t\, \mu\, G\left(-{}^{n}Y\left(\bar{\boldsymbol{\varepsilon}} + \mathbb{B}^{n}\tilde{\mathbf{U}}^{e} \right) \right) \right)}{1 + \Delta t\, \mu} - {}^{n}\omega = 0, \tag{36} $$

where $\Delta t = {}^{n}t - {}^{n-1}t$ is pseudo-time step. If $g < 0$, no further damage occurs and the local residual ${}^{n}H$ is simply

$$ {}^{n}H_{gp}\left({}^{n}\omega \right) = {}^{n-1}\omega - {}^{n}\omega = 0. \tag{37} $$

Ultimately, the ${}^{n}H_{gp} = 0$ equation is solved at the local level, i.e, at each Gauss point in the mesh. Fortunately, these scaler equations are not coupled.

Upon evaluating ${}^{n}\omega$ we compute the global tangent operator introduced in (31) by looping over all the element Gauss points as

$$ {}^{n}\mathbb{K} = \mathop{\mathbb{A}}_{e} \sum_{\text{Gauss points}} {}^{n}\mathbf{K}^{e}_{gp}, \tag{38} $$

where ${}^{n}\mathbf{K}^{e}_{gp}$ is the element Ω_e Gauss point tangent stiffness matrix

$$ {}^{n}\mathbf{K}^{e}_{gp} = \frac{\partial^{n}\mathbf{R}_{gp}}{\partial^{n}\tilde{\mathbf{U}}^{e}} - \frac{\partial^{n}\mathbf{R}_{gp}}{\partial^{n}\omega} \left(\frac{\partial^{n}H_{gp}}{\partial^{n}\omega} \right)^{-1} \frac{\partial^{n}H_{gp}}{\partial^{n}\tilde{\mathbf{U}}^{e}}. \tag{39} $$

In (39), the operators $\frac{\partial^n \mathbf{R}_{gp}}{\partial^n \tilde{\mathbf{U}}^e}$, $\frac{\partial^n \mathbf{R}_{gp}}{\partial^n \omega}$, $\frac{\partial^n H_{gp}}{\partial^n \omega}$, and $\frac{\partial^n H_{gp}}{\partial^n \tilde{\mathbf{U}}^e}$ are computed as

$$
\begin{aligned}
\frac{\partial^n \mathbf{R}_{gp}}{\partial^n \tilde{\mathbf{U}}^e} &= \mathbb{B}^T \left(1 -^n \omega\right) \mathbf{D}_0 \mathbb{B} w |\mathbf{J}|, \\
\frac{\partial^n \mathbf{R}_{gp}}{\partial^n \omega} &= -\mathbb{B}^T \mathbf{D}_0 \left(\bar{\boldsymbol{\varepsilon}} + \mathbb{B}^n \tilde{\mathbf{U}}^e\right) w |\mathbf{J}|, \\
\frac{\partial^n H_{gp}}{\partial^n \omega} &= -1, \\
\frac{\partial^n H_{gp}}{\partial^n \tilde{\mathbf{U}}^e} &= \begin{cases} -\dfrac{\Delta t\, \mu}{1 + \Delta t\, \mu} \dfrac{\partial G}{\partial^n Y} \left(\bar{\boldsymbol{\varepsilon}} + \mathbb{B}^n \tilde{\mathbf{U}}^e\right)^T \mathbf{D}_0 \mathbb{B} & \text{if } g \geq 0, \\ [\mathbf{0}] & \text{if } g < 0, \end{cases}
\end{aligned}
\tag{40}
$$

where $\bar{\boldsymbol{\varepsilon}}$ is the macroscopic strain introduced in (4).

Ultimately the global tangent operator (38) is used in (31) to evaluate the incremental perturbation displacement $\delta\tilde{\mathbf{U}}$.

5. OPTIMIZATION PROBLEM AND SENSITIVITY ANALYSIS

Our optimization problem is stated in mathematical form as

$$
\min_{\mathbf{d}} h_0 \left({}^0\mathbb{U}(\mathbf{X}(\mathbf{d}), \mathbf{d}),\, {}^0\mathbb{W}(\mathbf{X}(\mathbf{d}), \mathbf{d}),\, ...,\, {}^{N_f}\mathbb{U}(\mathbf{X}(\mathbf{d}), \mathbf{d}), {}^{N_f}\mathbb{W}(\mathbf{X}(\mathbf{d}), \mathbf{d}), \mathbf{X}(\mathbf{d}),\, \mathbf{d}\right),
$$

such that $\mathbf{d}^{lb} \leq \mathbf{d} \leq \mathbf{d}^{ub}$,

$$
h_j \left({}^0\mathbb{U}(\mathbf{X}(\mathbf{d}), \mathbf{d}),\, {}^0\mathbb{W}(\mathbf{X}(\mathbf{d}), \mathbf{d}),\, ...,\, {}^{N_f}\mathbb{U}(\mathbf{X}(\mathbf{d}), \mathbf{d}), {}^{N_f}\mathbb{W}(\mathbf{X}(\mathbf{d}), \mathbf{d}),\, \mathbf{X}(\mathbf{d}),\, \mathbf{d}\right) \leq 0,
\tag{41}
$$

for $j = 1,\, 2,\, ...,\, nc$, where h_0 is the objective functional, h_j denotes the nc inequality constraint functionals, $\mathbf{X}$ denotes the mesh nodal coordinate vector, and $\mathbf{d}$ is the design variable vector, subjected to the lower and upper bounds $\mathbf{d}^{lb}$ and $\mathbf{d}^{ub}$. The design variables describe the inclusion geometrical parameters and the material properties that ultimately determine the homogenized response of the composite material.

We solve the optimization problem (41) via a gradient-based approach to efficiently search the design space for the optimal solution, and thus we must provide the sensitivity of the objective and

constraints functions. And because the design variables describe both geometry and material, we must compute both shape and material sensitivities. The path-dependent nature of the nonlinear problems of interest are accommodated by utilizing the path-dependent direct differentiation sensitivity analysis in [95] and the shape sensitivity is obtained by using the development in [72].

To present the sensitivity analysis, let us redefine the objective and constraint functionals by considering only the terminal responses for conciseness as

$$\mathcal{F}(\mathbf{d}) = h_j\left({}^{N_f}\mathbb{U}^I(\mathbf{X}(\mathbf{d}),\mathbf{d}),\,{}^{N_f}\mathbb{W}^I(\mathbf{X}(\mathbf{d}),\mathbf{d}),\,\mathbf{X}(\mathbf{d})\right) \quad \text{for } j=0,\,1,\,...,\,nc. \tag{42}$$

For shape parameter d_i, the sensitivity of the functional expressed in (42) takes the form

$$\frac{d\mathcal{F}}{dd_i} = \left(\frac{\partial h_j}{\partial {}^{N_f}\mathbb{U}}\right)^T {}^{N_f}\overset{*}{\mathbb{U}}_i + \left(\frac{\partial h_j}{\partial {}^{N_f}\mathbb{W}}\right)^T {}^{N_f}\overset{*}{\mathbb{W}}_i + \left(\frac{\partial h_j}{\partial \mathbf{X}}\right)^T \mathbb{V}_i, \tag{43}$$

where $\overset{*}{\mathbb{U}}_i = \dfrac{\partial \mathbb{U}}{\partial \mathbf{X}}\mathbb{V}_i + \dfrac{\partial \mathbb{U}}{\partial d_i}$ and $\overset{*}{\mathbb{W}}_i = \dfrac{\partial \mathbb{W}}{\partial \mathbf{X}}\mathbb{V}_i + \dfrac{\partial \mathbb{W}}{\partial d_i}$ are the unknown material derivatives and $\mathbb{V}_i = \dfrac{\partial \mathbf{X}(\mathbf{d})}{\partial d_i}$ is the vector of nodal design velocities, i.e, the derivative of the node locations with respect to the design parameters. For the material parameters d_i, the sensitivity takes the simpler form:

$$\frac{d\mathcal{F}}{dd_i} = \left(\frac{\partial h_j}{\partial {}^{N_f}\mathbb{U}}\right)^T \frac{\partial {}^{N_f}\mathbb{U}}{\partial d_i} + \left(\frac{\partial h_j}{\partial {}^{N_f}\mathbb{W}}\right)^T \frac{\partial {}^{N_f}\mathbb{W}}{\partial d_i} + \frac{\partial h_j}{\partial d_i}. \tag{44}$$

For conciseness, we present hereafter only the details for the shape sensitivity (43).

To evaluate (43), we utilize the direct differentiation method wherein we compute the unknown material derivatives $\overset{*}{\mathbb{U}}_i$ and $\overset{*}{\mathbb{W}}_i$. To this end, we define the response fields $\mathbb{U}$ and $\mathbb{W}$ as functions of the design variable $\mathbf{d}$, and write (24) as

$$\begin{aligned} {}^{n}\mathbb{R}\left({}^{n}\mathbb{U}(\mathbf{X},\mathbf{d}),\,{}^{n-1}\mathbb{U}(\mathbf{X},\mathbf{d}),\,{}^{n}\mathbb{W}(\mathbf{X},\mathbf{d}),\,{}^{n-1}\mathbb{W}(\mathbf{X},\mathbf{d}),\,\mathbf{X}\right) &= \mathbf{0}, \\ {}^{n}\mathbb{H}\left({}^{n}\mathbb{U}(\mathbf{X},\mathbf{d}),\,{}^{n-1}\mathbb{U}(\mathbf{X},\mathbf{d}),\,{}^{n}\mathbb{W}(\mathbf{X},\mathbf{d}),\,{}^{n-1}\mathbb{W}(\mathbf{X},\mathbf{d}),\,\mathbf{X}\right) &= \mathbf{0}, \end{aligned} \tag{45}$$

where it is understood that $\mathbf{X}$ is a function of $\mathbf{d}$. To evaluate the implicit response sensitivities ${}^{N_f}\overset{*}{\mathbb{U}}_i$ and ${}^{N_f}\overset{*}{\mathbb{W}}_i$, we differentiate the residuals (45) with respect to design variable d_i as

$$\begin{cases} \frac{\partial^{N_f}\mathbb{R}}{\partial^{N_f}\mathbb{U}}{}^{N_f}\overset{*}{\mathbb{U}}_i + \frac{\partial^{N_f}\mathbb{R}}{\partial^{N_f-1}\mathbb{U}}{}^{N_f-1}\overset{*}{\mathbb{U}}_i + \frac{\partial^{N_f}\mathbb{R}}{\partial^{N_f}\mathbb{W}}{}^{N_f}\overset{*}{\mathbb{W}}_i + \frac{\partial^{N_f}\mathbb{R}}{\partial^{N_f-1}\mathbb{W}}{}^{N_f-1}\overset{*}{\mathbb{W}}_i + \frac{\partial^{N_f}\mathbb{R}}{\partial\mathbf{X}}\mathbb{V}_i = \mathbf{0} \\ \frac{\partial^{N_f}\mathbb{H}}{\partial^{N_f}\mathbb{U}}{}^{N_f}\overset{*}{\mathbb{U}}_i + \frac{\partial^{N_f}\mathbb{H}}{\partial^{N_f-1}\mathbb{U}}{}^{N_f-1}\overset{*}{\mathbb{U}}_i + \frac{\partial^{N_f}\mathbb{H}}{\partial^{N_f}\mathbb{W}}{}^{N_f}\overset{*}{\mathbb{W}}_i + \frac{\partial^{N_f}\mathbb{H}}{\partial^{N_f-1}\mathbb{W}}{}^{N_f-1}\overset{*}{\mathbb{W}}_i + \frac{\partial^{N_f}\mathbb{H}}{\partial\mathbf{X}}\mathbb{V}_i = \mathbf{0} \end{cases}. \tag{46}$$

Rearranging the second equation of (46), we detain an expression for ${}^{N_f}\overset{*}{\mathbb{W}}_i$ in terms of ${}^{N_f}\overset{*}{\mathbb{U}}_i$ as

$$\left(\frac{\partial^{N_f}\mathbb{H}}{\partial^{N_f}\mathbb{W}}\right){}^{N_f}\overset{*}{\mathbb{W}}_i = \left[\frac{\partial^{N_f}\mathbb{H}}{\partial^{N_f}\mathbb{U}}{}^{N_f}\overset{*}{\mathbb{U}}_i + \frac{\partial^{N_f}\mathbb{H}}{\partial^{N_f-1}\mathbb{U}}{}^{N_f-1}\overset{*}{\mathbb{U}}_i + \frac{\partial^{N_f}\mathbb{H}}{\partial^{N_f-1}\mathbb{W}}{}^{N_f-1}\overset{*}{\mathbb{W}}_i + \frac{\partial^{N_f}\mathbb{H}}{\partial\mathbf{X}}\mathbb{V}_i\right], \tag{47}$$

where $\dfrac{\partial^{N_f}\mathbb{H}}{\partial^{N_f}\mathbb{W}}$ is the local tangent operator used in the inner loop of the Newton-Raphson algorithm (29), and the term in the bracket on the right-hand side is referred to as the "local pseudo-load".

Substituting ${}^{N_f}\overset{*}{\mathbb{W}}_i$ from (47) into the first equation of (46) results in the following "global pseudo problem"

$$\begin{aligned}\left[\frac{\partial^{N_f}\mathbb{R}}{\partial^{N_f}\mathbb{U}} - \frac{\partial^{N_f}\mathbb{R}}{\partial^{N_f}\mathbb{W}}\left(\frac{\partial^{N_f}\mathbb{H}}{\partial^{N_f}\mathbb{W}}\right)^{-1}\frac{\partial^{N_f}\mathbb{H}}{\partial^{N_f}\mathbb{U}}\right]{}^{N_f}\overset{*}{\mathbb{U}}_i = &-\left[\frac{\partial^{N_f}\mathbb{R}}{\partial^{N_f-1}\mathbb{U}}{}^{N_f-1}\overset{*}{\mathbb{U}}_i + \frac{\partial^{N_f}\mathbb{R}}{\partial^{N_f-1}\mathbb{W}}{}^{N_f-1}\overset{*}{\mathbb{W}}_i\right. \\ &+\frac{\partial^{N_f}\mathbb{R}}{\partial\mathbf{X}}\mathbb{V}_i - \frac{\partial^{N_f}\mathbb{R}}{\partial^{N_f}\mathbb{W}}\left(\frac{\partial^{N_f}\mathbb{H}}{\partial^{N_f}\mathbb{W}}\right)^{-1} \\ &\times\left(\frac{\partial^{N_f}\mathbb{H}}{\partial^{N_f-1}\mathbb{U}}{}^{N_f-1}\overset{*}{\mathbb{U}}_i + \frac{\partial^{N_f}\mathbb{H}}{\partial^{N_f-1}\mathbb{W}}{}^{N_f-1}\overset{*}{\mathbb{W}}_i\right. \\ &\left.\left.+\frac{\partial^{N_f}\mathbb{H}}{\partial\mathbf{X}}\mathbb{V}_i\right)\right],\end{aligned} \tag{48}$$

where the left-hand side quantity in bracket is the global tangent operator introduced in the outer loop of the primal analysis (31) and the right-hand side forms the "global pseudo-load". After evaluating ${}^{N_f}\overset{*}{\mathbb{U}}_i$ from (48), ${}^{N_f}\overset{*}{\mathbb{W}}_i$ is obtained from (47). Note that in the pseudo problems we solve for $\overset{*}{\mathbb{U}}$ and then $\overset{*}{\mathbb{W}}$, but in the primal problems we first obtain $\mathbb{W}$ then $\mathbb{U}$.

Equations (47) and (48) contain the derivatives ${}^{N_f-1}\overset{*}{\mathbb{U}}_i$ and ${}^{N_f-1}\overset{*}{\mathbb{W}}_i$. But these are easily evaluated. Indeed, just as we march in time to evaluate ${}^{N_f}\mathbb{U}$ and ${}^{N_f}\mathbb{W}$, we march in time to evaluate ${}^{N_f}\overset{*}{\mathbb{U}}_i$ and ${}^{N_f}\overset{*}{\mathbb{W}}_i$. Starting from (46) we let ${}^{N_f}t \to {}^{1}t$ and use our knowledge of the initial

conditions ${}^{0}\overset{*}{\mathbb{U}}_i = \mathbf{0}$ and ${}^{0}\overset{*}{\mathbb{W}}_i = \mathbf{0}$ to evaluate ${}^{1}\overset{*}{\mathbb{U}}_i$ and ${}^{1}\overset{*}{\mathbb{W}}_i$ by first evaluating the pseudo-load in (48) and computing the material derivative ${}^{1}\overset{*}{\mathbb{U}}_i$ using a back-substitution of the previously decomposed global tangent stiffness matrix of (38). We then compute ${}^{1}\overset{*}{\mathbb{W}}_i$ by solving the local pseudo problem (47) at each Gauss point. We then proceed to time ${}^{2}t$ using our knowledge of ${}^{1}\overset{*}{\mathbb{U}}_i$ and ${}^{1}\overset{*}{\mathbb{W}}_i$ to evaluate ${}^{2}\overset{*}{\mathbb{U}}_i$ and ${}^{2}\overset{*}{\mathbb{W}}_i$ and so on. So the analysis for $\mathbb{U}$ and $\mathbb{W}$ and the sensitivity analysis for $\overset{*}{\mathbb{U}}_i$ and $\overset{*}{\mathbb{W}}_i$ are performed in tandem. At each time step ${}^{n}t$ we evaluate ${}^{n}\mathbb{U}$ and ${}^{n}\mathbb{W}$ and then their sensitivities ${}^{n}\overset{*}{\mathbb{U}}_i$ and ${}^{n}\overset{*}{\mathbb{W}}_i$. Finally, we evaluate $\mathcal{F}$ and $\dfrac{d\mathcal{F}}{dd_i}$ from (42) and (43), respectively.

As depicted in Figure 1, the objective of our optimization problem is to obtain the desired macroscopic material response by minimizing the objective function

$$h_0(\mathbf{d}) = \frac{\int_0^{\bar{\varepsilon}_{\max}} \left\| \bar{\boldsymbol{\sigma}}(\bar{\varepsilon}, \mathbf{d}) - \boldsymbol{\sigma}^{\text{desired}}(\bar{\varepsilon}) \right\|^2 d\bar{\varepsilon}}{\int_0^{\bar{\varepsilon}_{\max}} \left\| \boldsymbol{\sigma}^{\text{desired}}(\bar{\varepsilon}) \right\|^2 d\bar{\varepsilon}}. \tag{49}$$

To perform the sensitivity analysis, the global pseudo-loads introduced in (48) at the loading step ${}^{n}t$ are evaluated by assembling the element Ω_e pseudo-load vectors that are computed by summing over the Gauss points,

$${}^{n}\mathbb{P}^{i}_{ps} = \mathop{\mathbb{A}}_{e} \sum_{\text{Gauss points}} {}^{n}\mathbf{P}^{e}_{gp}, \tag{50}$$

where ${}^{n}\mathbf{P}^{e}_{gp}$ is determined for each finite element Gauss point as

$$\begin{aligned} {}^{n}\mathbf{P}^{e}_{gp} = -\Bigg[& \frac{\partial^n \mathbf{R}_{gp}}{\partial^{n-1}\tilde{\mathbf{U}}^e} {}^{n-1}\overset{*}{\tilde{\mathbf{U}}}^{e}_{i} + \frac{\partial^n \mathbf{R}_{gp}}{\partial^{n-1}\omega} {}^{n-1}\overset{*}{\omega}_i + \frac{\partial^n \mathbf{R}_{gp}}{\partial \mathbf{X}^e} \mathbb{V}^e_i - \frac{\partial^n \mathbf{R}_{gp}}{\partial^n \omega} \left(\frac{\partial^n H_{gp}}{\partial^n \omega} \right)^{-1} \\ & \times \left(\frac{\partial^n H_{gp}}{\partial^{n-1}\tilde{\mathbf{U}}^e} {}^{n-1}\overset{*}{\tilde{\mathbf{U}}}^{e}_{i} + \frac{\partial^n H_{gp}}{\partial^{n-1}\omega} {}^{n-1}\overset{*}{\omega}_i + \frac{\partial^n H_{gp}}{\partial \mathbf{X}^e} \mathbb{V}^e_i \right) \Bigg] w|\mathbf{J}|. \end{aligned} \tag{51}$$

In (51), $\mathbf{R}_{gp}$ and H_{gp} are the global and local Gauss point residuals introduced in (34) and (36), respectively. The operators $\dfrac{\partial^n \mathbf{R}_{gp}}{\partial^{n-1}\tilde{\mathbf{U}}^e}$, $\dfrac{\partial^n \mathbf{R}_{gp}}{\partial^{n-1}\omega}$, and $\dfrac{\partial^n H_{gp}}{\partial^{n-1}\tilde{\mathbf{U}}^e}$ vanish owing to the definition of $\mathbf{R}_{gp}$ and H_{gp}, and the operators $\dfrac{\partial^n \mathbf{R}_{gp}}{\partial^n \tilde{\mathbf{U}}^e}$, $\dfrac{\partial^n \mathbf{R}_{gp}}{\partial^n \omega}$, $\dfrac{\partial^n H_{gp}}{\partial^n \omega}$, and $\dfrac{\partial^n H_{gp}}{\partial^n \tilde{\mathbf{U}}^e}$ are defined in (40). The operator $\dfrac{\partial^n H_{gp}}{\partial^{n-1}\omega}$ is expressed as

$$\frac{\partial^n H_{gp}}{\partial^{n-1}\omega} = \begin{cases} \dfrac{1}{1+\Delta t \mu} & \text{if } g \geq 0, \\ 1 & \text{if } g < 0. \end{cases} \tag{52}$$

The quantity $\frac{\partial^n \mathbf{R}_{gp}}{\partial \mathbf{X}^e}\mathbb{V}_i^e$, which is nonzero over the enriched elements, is

$$\frac{\partial^n \mathbf{R}}{\partial \mathbf{X}^e}\mathbb{V}_i^e = \overset{*}{\mathbb{B}}_i^T \left(1 - {}^n\omega\right)\mathbf{D}_0\left(\bar{\boldsymbol{\varepsilon}} + \mathbb{B}\,{}^n\tilde{\mathbf{U}}^e\right) + \begin{bmatrix} \tilde{\mathbf{M}}_{11} & \tilde{\mathbf{M}}_{12} \\ \left(\tilde{\mathbf{M}}_{12}\right)^T & \tilde{\mathbf{M}}_{22} \end{bmatrix} \begin{bmatrix} {}^n\tilde{\mathbf{U}}_p^e \\ {}^n\tilde{\mathbf{U}}_\psi^e \end{bmatrix} \tag{53}$$
$$+ \mathbb{B}^T \left(1 - {}^n\omega\right)\mathbf{D}_0\left(\bar{\boldsymbol{\varepsilon}} + \mathbb{B}\,{}^n\tilde{\mathbf{U}}^e\right)\mathrm{vec}\left(\mathbf{I}\right)^T \mathbb{B}\mathbb{V}_i^e,$$

where vec (I) is the vector of Identity matrix, and the $\tilde{\mathbf{M}}_{ij}$ matrices entering (53) are given by

$$\begin{aligned}
\tilde{\mathbf{M}}_{11} &= \left[\mathbf{B}_N^T \left(1 - {}^n\omega\right)\mathbf{D}_0 \overset{*}{\mathbf{B}}_{Ni} + \overset{*}{\mathbf{B}}_{Ni}^T \left(1 - {}^n\omega\right)\mathbf{D}_0\mathbf{B}_N\right], \\
\tilde{\mathbf{M}}_{12} &= \left[\mathbf{B}_N^T \left(1 - {}^n\omega\right)\mathbf{D}_0 \overset{*}{\mathbf{B}}_{\psi i} + \overset{*}{\mathbf{B}}_{Ni}^T \left(1 - {}^n\omega\right)\mathbf{D}_0\mathbf{B}_\psi\right], \\
\tilde{\mathbf{M}}_{22} &= \left[\mathbf{B}_\psi^T \left(1 - {}^n\omega\right)\mathbf{D}_0 \overset{*}{\mathbf{B}}_{\psi i} + \overset{*}{\mathbf{B}}_{\psi i}^T \left(1 - {}^n\omega\right)\mathbf{D}_0\mathbf{B}_\psi\right].
\end{aligned} \tag{54}$$

In (53), ${}^n\tilde{\mathbf{U}}_\psi^e$ is the perturbation displacement associated with the enriched dofs added to the element along the material interface, and ${}^n\tilde{\mathbf{U}}_p^e$ is the perturbation displacement of the original nodes (Figure 2(d)). Combining these two terms, we have the element perturbation displacement ${}^n\tilde{\mathbf{U}}^e = \begin{bmatrix} \left({}^n\tilde{\mathbf{U}}_p^e\right)^T & \left({}^n\tilde{\mathbf{U}}_\psi^e\right)^T \end{bmatrix}^T$. The matrices $\mathbb{B}$, $\mathbf{B}_N$, and $\mathbf{B}_\psi$ and their derivatives $\overset{*}{\mathbb{B}}_i$, $\overset{*}{\mathbf{B}}_{Ni}$, and $\overset{*}{\mathbf{B}}_\psi$ appearing in (53) and (54), are provided in Appendix B and [72].

The term $\mathrm{vec}\left(\mathbf{I}\right)^T \mathbb{B}\mathbb{V}_i^e$ in (53) is the divergence of shape velocity field. More details for computing the shape velocity are presented in Appendix F and [72].

The Gauss point operator $\frac{\partial^n H_{gp}}{\partial \mathbf{X}^e}\mathbb{V}_i^e$ appearing in (51) is computed as

$$\frac{\partial^n H_{gp}}{\partial \mathbf{X}^e}\mathbb{V}_i^e = \begin{cases} -\dfrac{\Delta t\,\mu}{1 + \Delta t\,\mu}\dfrac{\partial G}{\partial {}^nY}\left(\bar{\boldsymbol{\varepsilon}} + \mathbb{B}\,{}^n\tilde{\mathbf{U}}^e\right)^T \mathbf{D}_0 \overset{*}{\mathbb{B}}_i {}^n\tilde{\mathbf{U}}^e & \text{if } g \geq 0, \\ 0 & \text{if } g < 0. \end{cases} \tag{55}$$

6. VERIFICATION EXAMPLES

In this section, we present a number of problems involving the design of composite materials exhibiting linear and nonlinear behaviors. In the first example, we design a 3D linear structure to

verify the proposed NIGFEM shape optimization scheme. In the next examples, we demonstrate the multilevel framework to design composite materials. In these verification case studies, we design to a macroscopic stress-strain curve associated with a particular inclusion configuration. In this way, we guarantee that the optimal objective function value equals zero.

6.1. Optimal design of an ellipsoidal inclusion subjected to uniaxial loading

In this first example, we find the shape of an ellipsoidal inclusion embedded in a cube domain subjected to uniaxial tension σ_{xx} to minimize the compliance of structure. As depicted in Figure 3, the domain is an L^3 cube with ellipsoidal inclusion, that is stiffer than the surrounding matrix ($E_2/E_1 = 30$ and $\nu_1 = 1.5\nu_2$). The design variables are the lengths and orientations of the three ellipsoid axes. The range of the three ellipsoid axes are $0.2L \leq a \leq 0.4L$, $0.1L \leq b \leq 0.3L$, $0.05L \leq c \leq 0.25L$ and their angles are limited to $[0, \pi/2]$. A maximum inclusion volume ($V \leq 4/3 \times \pi \times (0.3L)^3 = 0.1131L^3$) constrains the optimization problem. Owing to the loading condition and the material mismatch between the inclusion and the matrix, we expect the ellipsoidal inclusion to attain the maximum allowable volume and orient its major principal axis in the loading direction. Starting far from optimal point (Figure 3(c)), the compliance gets minimized in few iterations by moving to the expected optimal design (Figure 3(d)), whereas the volume constraint is satisfied as shown in Figure 3(b).

6.2. A unit cell with two inclusions subjected to macroscopic pure shear strain

In this example, we couple our shape optimization method with computational homogenization to design the composite microstructure to obtain a desired macroscopic shear stress when subjected to a macroscopic pure shear strain $\bar{\varepsilon}_{xy}$. The design domain is the periodic L^3 unit cell with two inclusions as shown in Figure 4. To model the unit cell, we use a 3D finite element mesh that has one element in the thickness direction. We assume damage only occurs in the inclusions. As illustrated in Figure 1(b), the optimization goal is to find the radii and locations of the circular inclusions to achieve the macroscopic stress-strain curve depicted by a red solid curve in Figure 5. The objective function for this example is defined by (49) wherein the trapezoidal rule is used to compute the

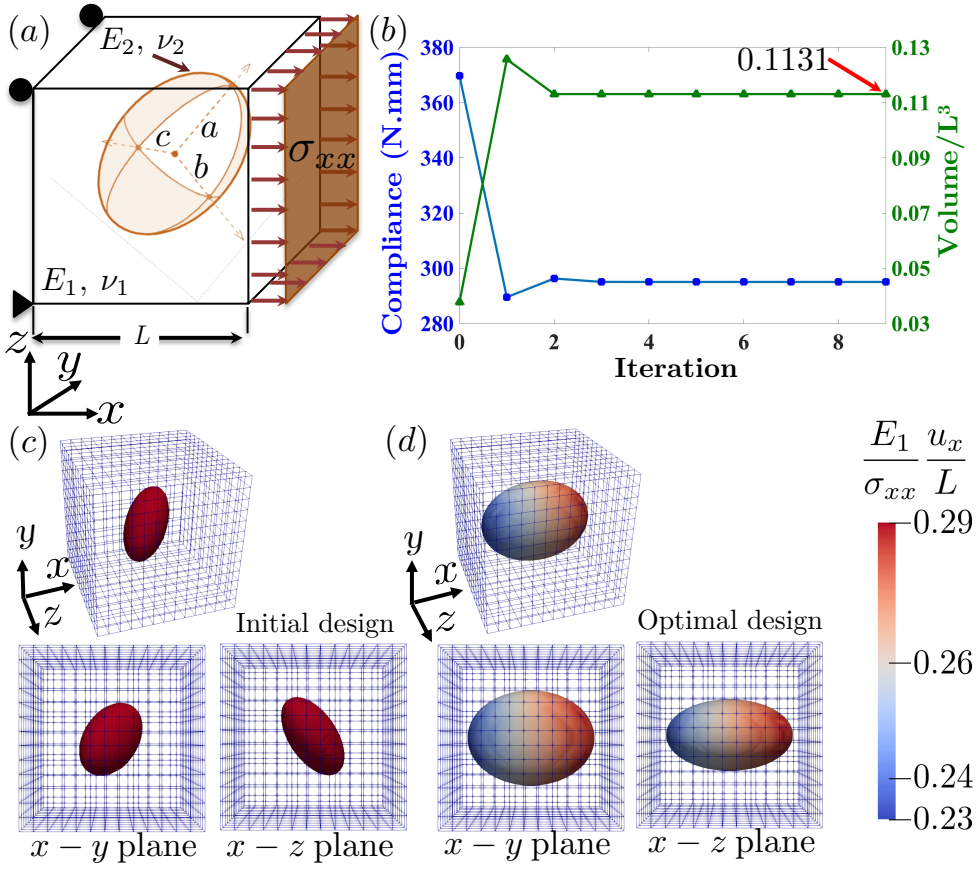

Figure 3. Shape optimization of a stiff ellipsoidal inclusion embedded in a cubic domain subjected to an uniaxial loading: (a) problem description; (b) convergence history of the structure compliance and the inclusion volume fraction constraint; (c and d) initial and optimal designs. The contours represent the normalized displacement in the x-direction over the inclusion surface.

integrals. To prevent the inclusions from overlapping, we constrain the distance C_{ij} between the centers of inclusions i and j such that $C_{ij} \geq R_i + R_j + 0.08L$, where R_i denotes the inclusions' radii. We also define additional constraints that ensure the inclusions are wholly inside the domain.

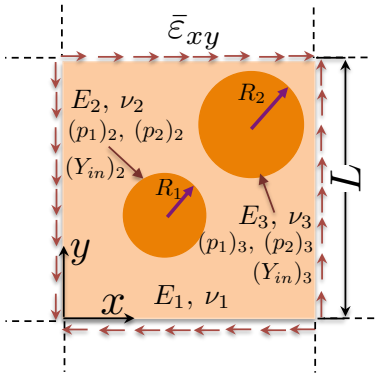

Figure 4. Multiscale design of a nonlinear composite: periodic unit cell including two inclusions. The design variables are the size (radius) and center location of inclusions.

To model the isotropic constituent materials, we use $E_2 = 10E_1 = 100E_3 = 100$ GPa and $\nu_1 = 0.22$ and $\nu_2 = \nu_3 = 0.34$. We also assign $p_1 = 10$, $p_2 = 1$, and $\mu = 20S^{-1}$ for both inclusions, but $(Y_{in})_3 = 10(Y_{in})_2 = 500$ Pa, cf. (18). The desired stress-strain response is associated with inclusion 1 located at: $X_{c1} = 0.35$, $Y_{c1} = 0.65$ with $R_1 = 0.25$, and inclusion 2 located at: $X_{c2} = 0.75$, $Y_{c2} = 0.25$, with $R_2 = 0.15$.

Figure 5 presents stress-strain curves for a few selected iterations. We observe that, although we start far from the desired response, the optimizer quickly converges to the desired macroscopic stress-strain curve. Figure 6 presents the results obtained for five different initial designs and shows that all converge to optimized microstructure configurations with the same desired macroscopic nonlinear response. As illustrated in Figure 6, the different optimized configurations actually represent one unique microstructure, but for a transformed unit cell. Specifically, there are four different inclusion configurations that produce the desired nonlinear response due to the periodicity of the unit cell, which is subjected to macroscopic pure shear strain. Figure 7 illustrates the deformed and undeformed shapes of the initial and optimized periodic unit cells for the design 3 of Figure 6.

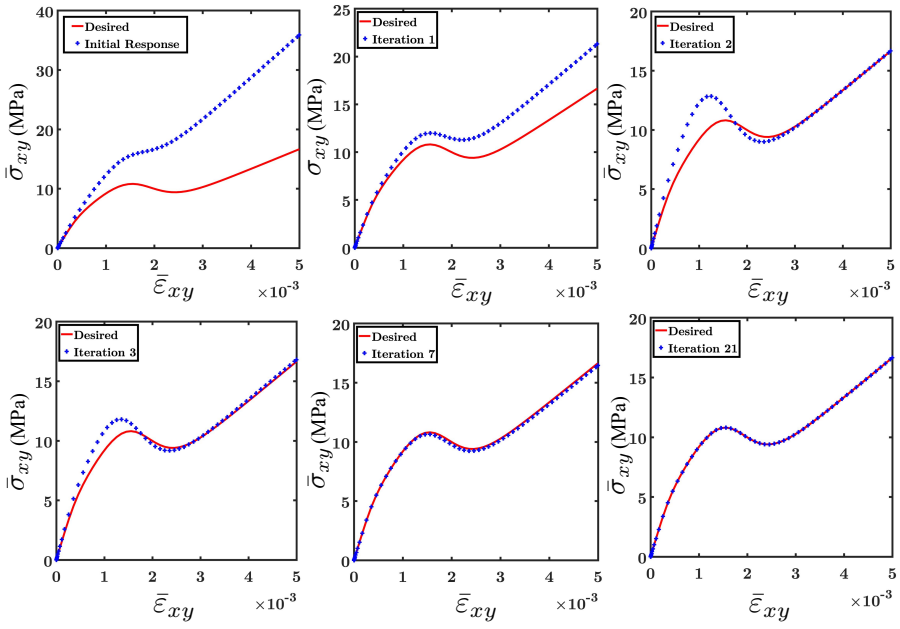

Figure 5. Stress-strain curves for some selected iterations. The desired response is shown by a solid curve, while the computed (designed) response is denoted with symbols.

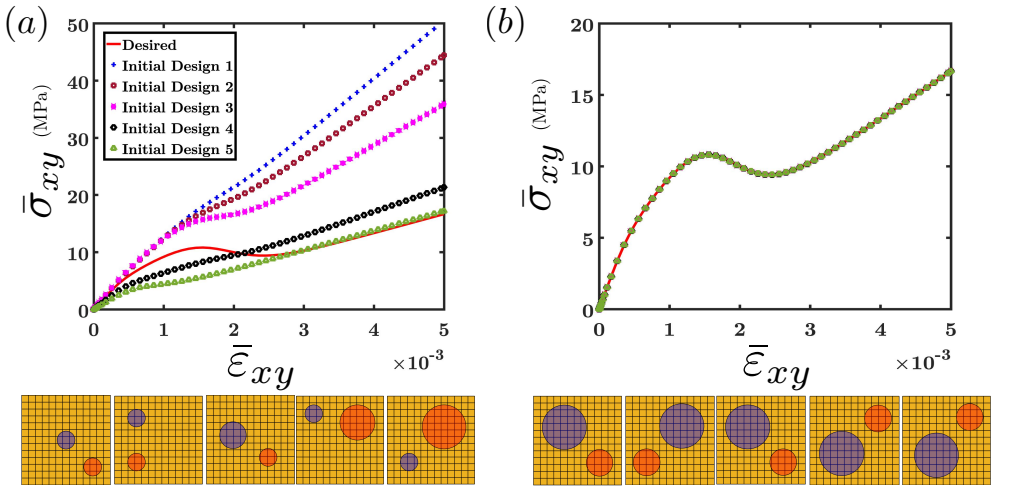

Figure 6. Stress-strain curves for five different initial designs, (a) initial designs, (b) optimized designs. As apparent from the optimized designs, various optimized configurations satisfy the desired stress-strain response due to the periodicity of the unit cell.

Similar to the problem presented in Figure 4, Figure 8 shows an unit cell subjected to macroscopic pure shear $\bar{\varepsilon}_{xy}$, but with eight inclusions. The material properties of the matrix (E_1 and ν_1), the inclusions labeled by number 2 (E_2, ν_2, $(p_1)_2$, $(p_2)_2$, and $(Y_{in})_2$), and the inclusions labeled by number 3 (E_3, ν_3, $(p_1)_3$, $(p_2)_3$, and $(Y_{in})_3$) are the same as those for the previous study. We optimize the inclusions' radii and locations subject to the previously described constraints to obtain the desired stress-strain response represented by the solid red curve in the same figure. The size and location of inclusions associated with the desired stress-strain behavior are: ($X_{c1} = 0.15$, $Y_{c1} = 0.15, R_1 = 0.1$) , ($X_{c2} = 0.50, Y_{c2} = 0.20, R_2 = 0.15$), ($X_{c3} = 0.85, Y_{c3} = 0.20, R_3 = 0.09$), ($X_{c4} = 0.20$, $Y_{c4} = 0.47$, $R_4 = 0.12$), ($X_{c5} = 0.75$, $Y_{c5} = 0.50$, $R_5 = 0.10$), ($X_{c6} = 0.20$, $Y_{c6} = 0.80$, $R_6 = 0.12$), ($X_{c7} = 0.50$, $Y_{c7} = 0.80$, $R_7 = 0.09$), and ($X_{c8} = 0.80$, $Y_{c8} = 0.80$, $R_8 = 0.12$). The initial and optimized designs for this problem are also illustrated in the figure. As shown in Figure 8, the optimizer quickly converges to the desired macroscopic stress-strain curve.

6.3. A cubic unit cell with three spherical particles subjected to a macroscopic pure shear strain

The third verification example is the design of the three-dimensional L^3 unit cell with three spherical particles to obtain desired shear stress when subjected to a macroscopic pure shear strain $\bar{\varepsilon}_{xy}$

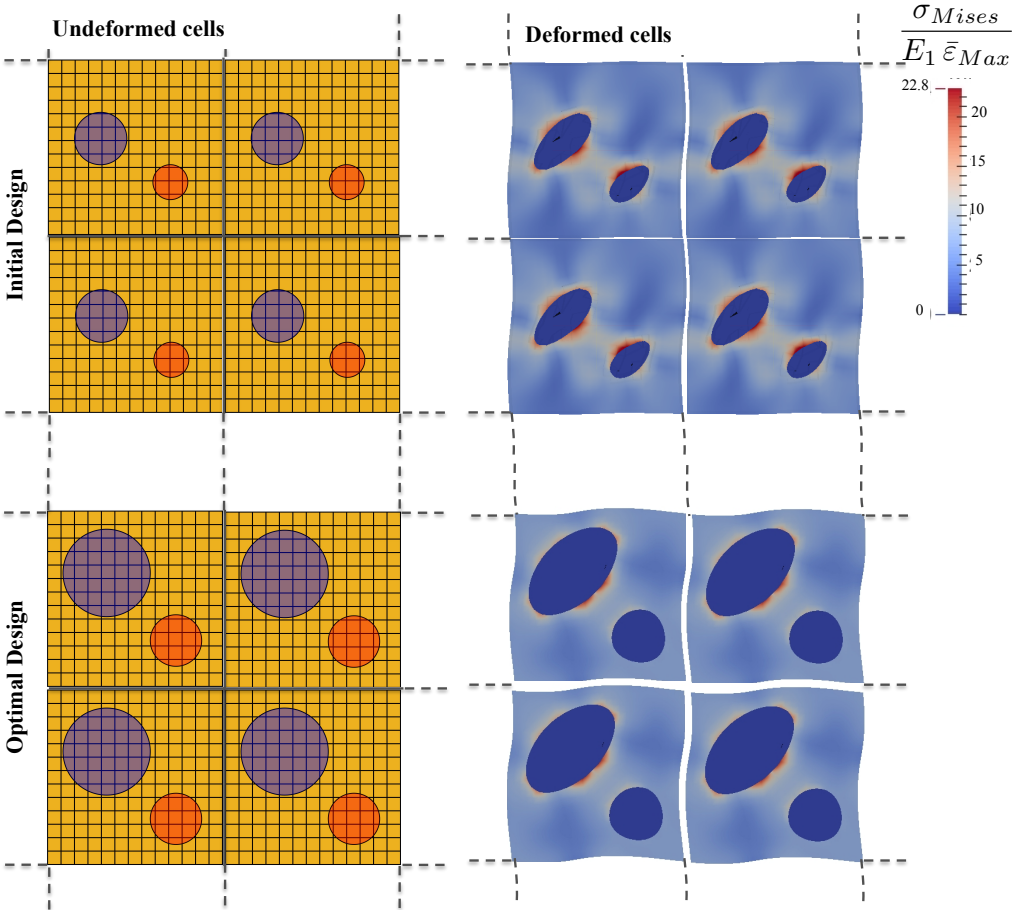

Figure 7. Deformed and undeformed shapes of the periodic unit cell for the initial and optimal designs associated with Figure 5. The contours indicate the normalized von Mises stress distribution in the unit cell.

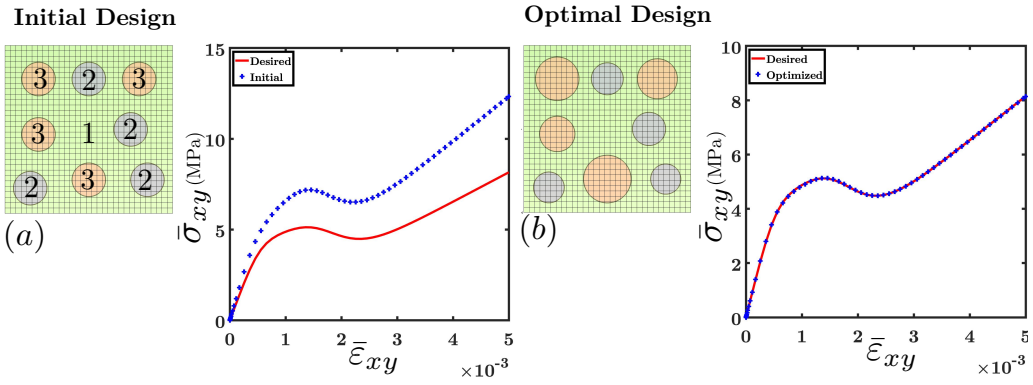

Figure 8. (a) Initial and (b) optimal designs and their associated macroscopic nonlinear responses for a unit cell with eight inclusions. The numbers 1, 2, and 3 identify the three different materials for the matrix and inclusions, respectively.

(Figure 9(a)). The damage is again limited to the particles and we again assume isotropy and use $E_2 = 10E_1 = 100E_3 = 100$ GPa, $\nu_1 = 0.22$, and $\nu_2 = \nu_3 = 0.34$. We also use $p_1 = 10$, $p_2 = 1$, and $\mu = 20S^{-1}$ for both inclusions, but $(Y_{in})_3 = 10(Y_{in})_2 = 500$ Pa. The total and perturbation displacement magnitudes in the periodic unit cell associated with the initial design are presented in Figs. 9(b) and (c), respectively. The goal of this example is to find the optimal inclusions' radii producing the desired macroscopic nonlinear stress-strain response shown with the red solid curve in Figure 10. Similar to all the verification examples, the desired stress-strain curve represents the nonlinear behavior of a particular inclusion distribution (i.e., $(X_{c1} = 0.158,\ Y_{c1} = 0.158,\ Z_{c1} = 0.158,\ R_1 = 0.08)$, $(X_{c2} = 0.53,\ Y_{c2} = 0.53,\ Z_{c2} = 0.53,\ R_2 = 0.15)$, and $(X_{c3} = 0.158,\ Y_{c3} = 0.158,\ Z_{c3} = 0.158,\ R_1 = 0.08)$). As shown in the figure, the optimized unit cell exhibits the desired response.

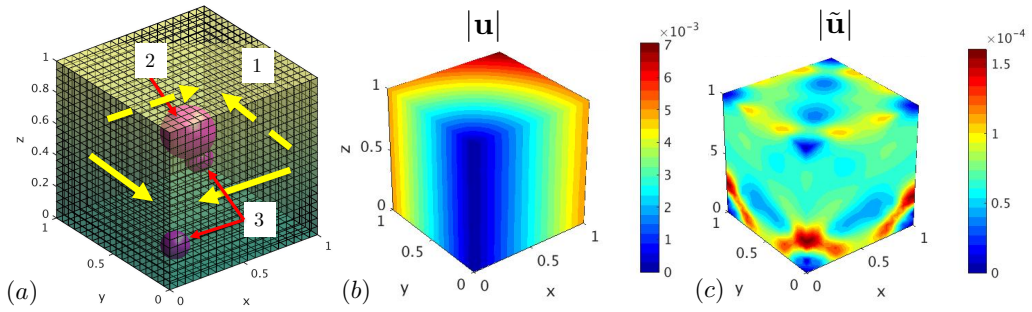

Figure 9. (a) 3D periodic unit cell with three spherical particles; (b) and (c) total and perturbation displacement magnitude in the unit cell subjected to a macroscopic pure shear strain $\bar{\varepsilon}_{xy}$ for the initial design. The displacements values are in mm.

7. APPLICATION EXAMPLES

We now apply the proposed multiscale optimization method to design microstructure for an arbitrary macroscale material response. In contrast to verification examples, in this section, we choose the desired macroscopic behaviors without any a priori knowledge. In particular, we select trilinear responses that resemble strain hardening, softening, and a "elastic-perfectly-plastic-like" behaviors, and our goal is to find the geometrical and material parameters of the microstructures to obtain these desired macroscopic behaviors.

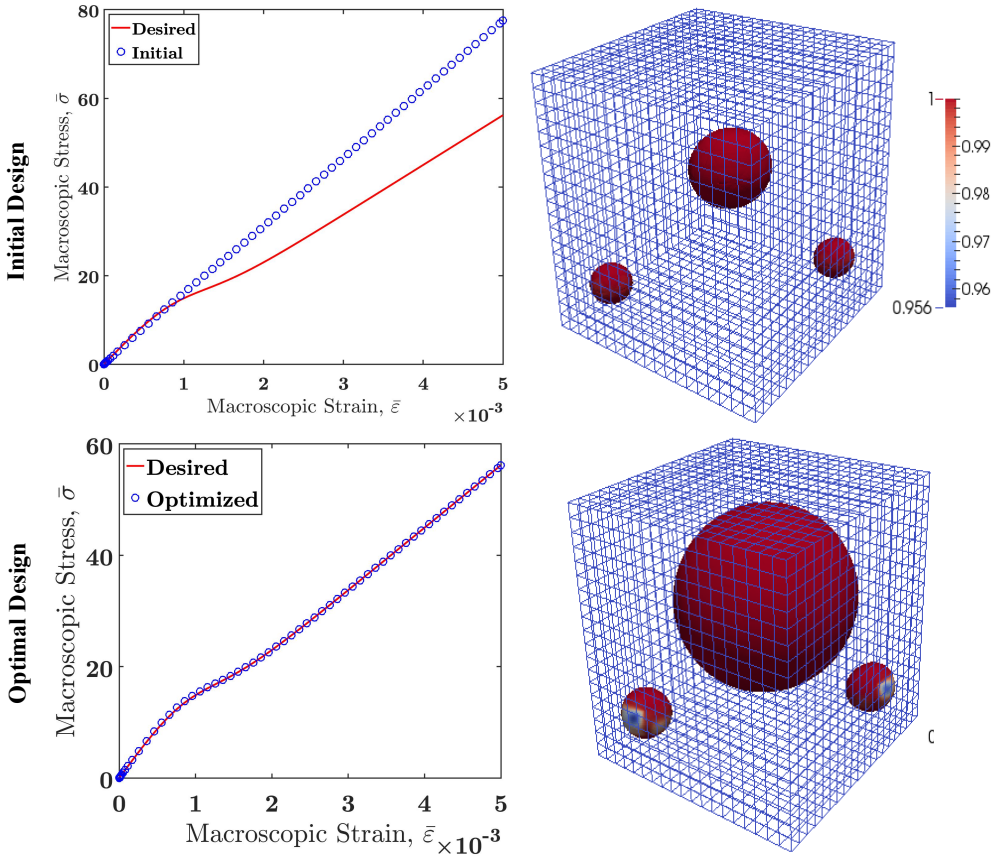

Figure 10. The initial (top) and optimal (bottom) designs for a 3D unit cell with three spherical inclusions. The contours show the damage variable ω in the inclusions.

7.1. Nonlinear multiscale design of a periodic composite for a desired macroscopic trilinear response

In the first application example, we optimize the two inclusions unit cell (cf. Figure 4) of Section 6.2 to obtain the desired trilinear response illustrated by the solid red curve in Figure 11(b). The optimized results appear in Figure 11. As shown in the Figure 11(b), starting far from the desired curve, the optimizer tries to approach to the desired curve while reducing the objective function. As apparent there, the final curve does not completely match to the desired response but it is very close to it.

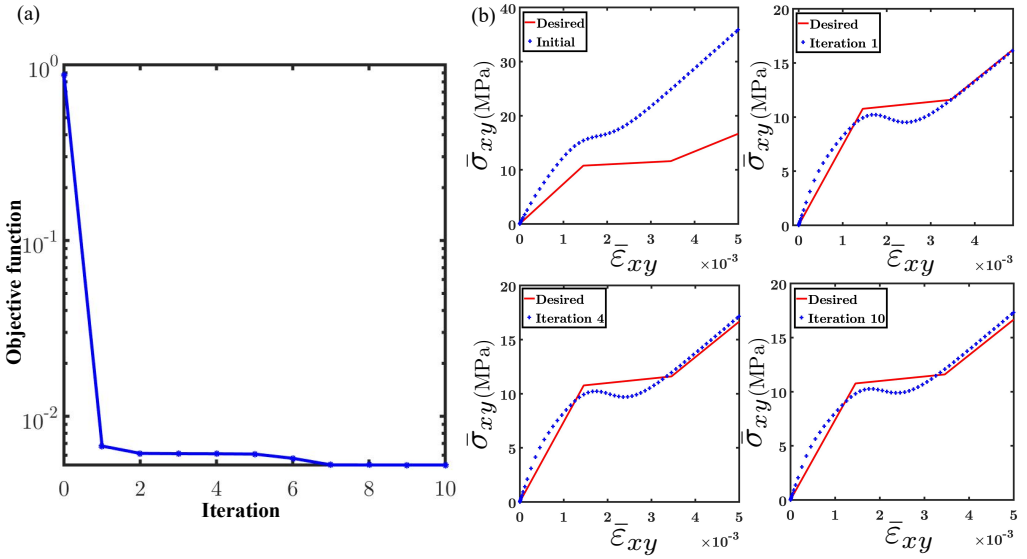

Figure 11. (a) Convergence history of the objective function defined in (49) for the Figure 6(a) design; (b) stress-strain curves for selected iterations. The desired response is shown with a solid curve, while the computed (designed) stress-strain curves are plotted with symbols.

7.2. Design of a periodic composite for a set of desired macroscopic trilinear stress-strain curves

In this example, we now design five different two inclusions periodic unit cells to achieve five different trilinear perfectly plastic macroscopic stress-strain curves[§§](Figure 12(a)). The unit cell is subjected to a macroscopic uniaxial strain $\bar{\varepsilon}_x$. In addition to the inclusion geometry, we also optimize the constituent properties. The initial material properties are assumed as $E_2 = 10E_1 = 100E_3 =$ 100 GPa, $\nu_1 = \nu_2 = \nu_3 = 0.34$, and $(Y_{in})_3 = 10(Y_{in})_2 = 600$ Pa. We also use $p_1 = 10$, $p_2 = 1$ and $\mu = 20s^{-1}$ for both inclusions. The macroscopic nonlinear response for the initial design is plotted in Figure 12(a) with blue circle symbols. Figure 12(b) shows how the stress-strain curves approaches the desired curves as the optimization converges to the designs depicted in Figure 12(d). The optimal design variable values are presented in Table I. As seen in the table, we allow the optimizer to find different material properties for each inclusion to achieve desired macroscopic stress-strain curves. Of course, we know the ability to assign properties to each individual inclusion is a difficult task, but with the ever increasing advancements in additive manufacturing technologies, this may be viable in the not so distant future.

[§§]Note that we do not consider any plastic behavior in this study and nonlinearity is introduced through an isotropic damage model.

Table I. Optimal design variables for five different desired trilinear stress-strain curves shown in Figure 12.

		R/L	X_c/L	Y_c/L	E (GPa)	Y_{in}(Pa)	p_1
Desired design 1	Inclusion 1	0.18	0.25	0.52	52.21	31.56	1.50
	Inclusion 2	0.18	0.74	0.35	4.59	902.54	2.96
Desired design 2	Inclusion 1	0.27	0.33	0.64	136.20	20.18	1.84
	Inclusion 2	0.18	0.74	0.25	0.5	119.53	0.1
Desired design 3	Inclusion 1	0.28	0.32	0.64	119.67	5.96	23.02
	Inclusion 2	0.18	0.73	0.28	0.5	50	0.1
Desired design 4	Inclusion 1	0.30	0.34	0.64	50	21.94	100
	Inclusion 2	0.18	0.75	0.26	0.5	100	0.1
Desired design 5	Inclusion 1	0.31	0.35	0.65	61.01	29.20	70.94
	Inclusion 2	0.18	0.75	0.25	0.90	156.49	0.44

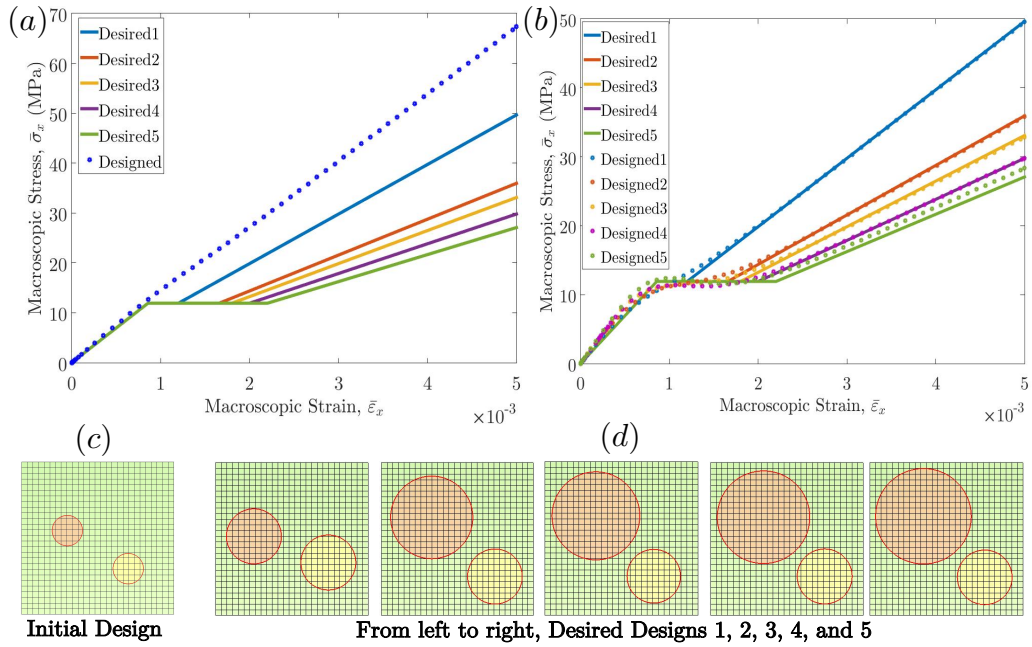

Figure 12. (a) Initial and desired stress-strain curves; (b) optimized and desired stress-strain curves; (c) initial and (d) optimized configurations of five two inclusions unit cells.

Now we repeat this example by replacing the perfectly plastic regions in the trilinear stress-strain curves with five different linear segments to resemble strain hardening and softening behaviors. Five optimized unit cells are designed for both the single and double inclusion cases. Results for the single inclusion case appear in Figure 13 and Table II. As apparent in the figure, the unit cell's responses with one inclusion are not capable of matching the desired stress-strain curves.

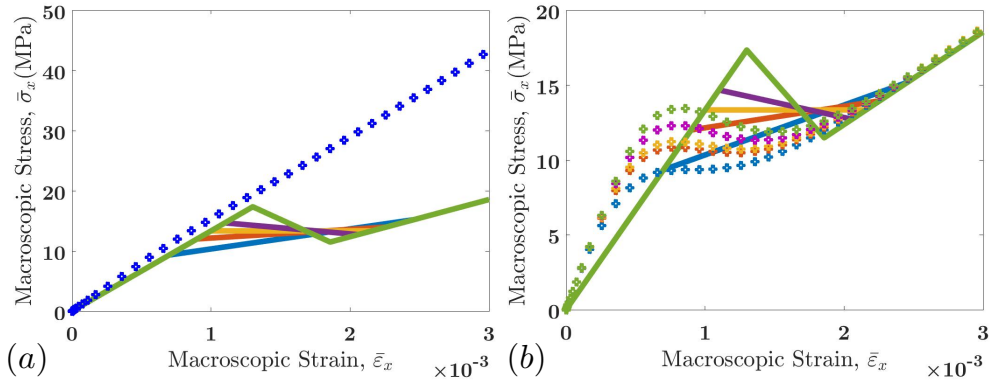

Figure 13. (a) Initial (dotted curve) and five desired stress-strain curves (solid curves) and (b) five optimized (dotted curve) and desired stress-strain curves for the single inclusion case.

Table II. Initial and optimal design variables for five different desired trilinear stress-strain curves shown in Figure 13.

	R/L	E (GPa)	Y_{in}(Pa)	p_1
Initial design	0.1	100	60	10
Desired design 1	0.34	50.00	17.85	8.04
Desired design 2	0.34	50.00	14.26	55.17
Desired design 3	0.34	50.00	34.91	26.84
Desired design 4	0.34	50.00	55.35	27.86
Desired design 5	0.34	50.00	31.31	75.22

Figure 14 and Table III show the results for the two inclusion cases. The optimized microstructures reasonably to capture to the desired trilinear stress-strain curves, except for the fifth curve that exhibits strain softening. A unit cell with more inclusions would be needed to capture this behavior.

7.3. A cubic unit cell with a spherical particles subjected to a macroscopic pure shear strain

The last example is the design of the 3-D cubic periodic unit cell of size L containing a spherical particle to obtain a pair of trilinear perfectly plastic macroscopic stress-strain responses (Figure 15). The unit cell is subjected to a macroscopic pure shear strain $\bar{\varepsilon}_{xy}$. The design parameters are the

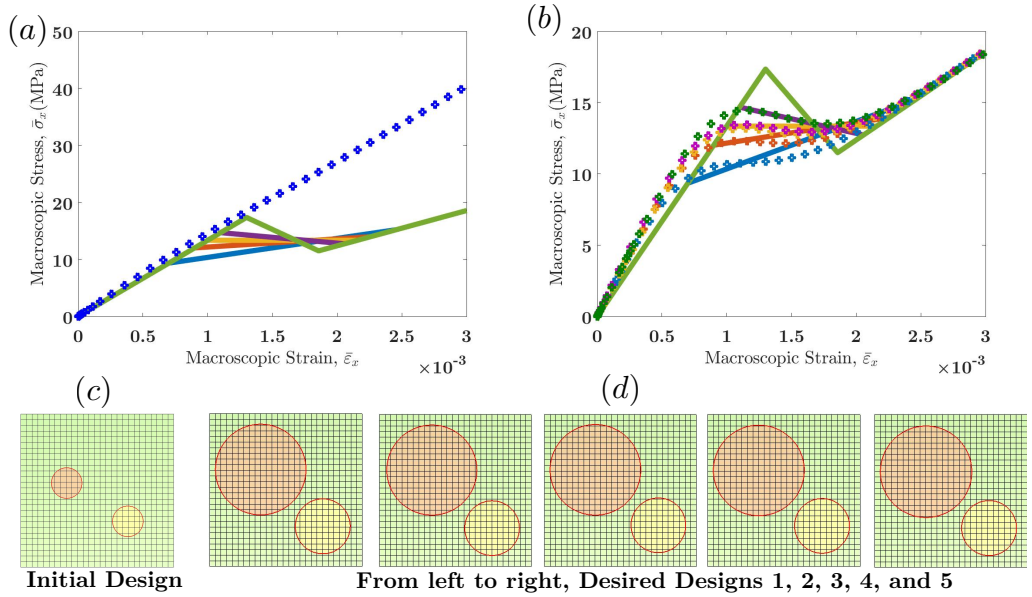

Figure 14. (a) Initial (dotted curve) and five desired stress-strain curves (solid curves) and (b) five optimized (dotted curve) and desired stress-strain curves for the double inclusion case; (c) initial and (d) final configurations of the unit cell containing two inclusions.

Table III. Initial and optimal design variables for five different desired trilinear stress-strain curves shown in Figure 14.

		R/L	X_c/L	Y_c/L	E (GPa)	Y_{in}(Pa)	p_1
Initial design	Inclusion 1	0.1	0.3	0.55	100	60	10
	Inclusion 2	0.1	0.7	0.3	1	600	10
Desired design 1	Inclusion 1	0.30	0.33	0.63	56.63	12.47	76.84
	Inclusion 2	0.18	0.74	0.26	0.50	50	0.10
Desired design 2	Inclusion 1	0.30	0.34	0.63	50	141.59	15.45
	Inclusion 2	0.18	0.74	0.25	0.5	115.11	30.72
Desired design 3	Inclusion 1	0.30	0.33	0.64	50	39.97	81.69
	Inclusion 2	0.18	0.75	0.27	0.50	100	0.10
Desired design 4	Inclusion 1	0.30	0.33	0.63	180.49	9.20	26.33
	Inclusion 2	0.18	0.75	0.27	0.50	50.09	0.10
Desired design 5	Inclusion 1	0.30	0.34	0.63	68.76	29.71	100
	Inclusion 2	0.18	0.75	0.26	0.50	130.75	0.10

inclusion's radius and the linear and nonlinear constituent properties. The inclusion's initial radius is $R_1 = 0.25$, and it is located at the center of the unit cell. The initial material properties are also assumed as $E_2 = 10E_1 = 100$ GPa, $\nu_1 = 0.22$, and $\nu_2 = 0.34$. We also consider $p_1 = 10$, $p_2 = 1$, and $\mu = 20S^{-1}$, and $Y_{in} = 50$ MPa for the inclusion damage parameters. The macroscopic material

nonlinear response associated with the initial design is illustrated In Figure 15(b) with blue circle markers. Figure 15(c) and (d) show stress-strain curves for some selected optimization iteration while the optimizer converges to the desired designs. The optimized design variable values are presented in Table IV. As seen in Figure 15(c) and (d), the unit cell with optimized microstructures capture the linear responses but is not able to capture the plateau associated with the transition. Similar to the example presented in Figure 14, a more complex unit cell containing more inclusions would be needed to achieve a closer match to the desired macroscopic response.

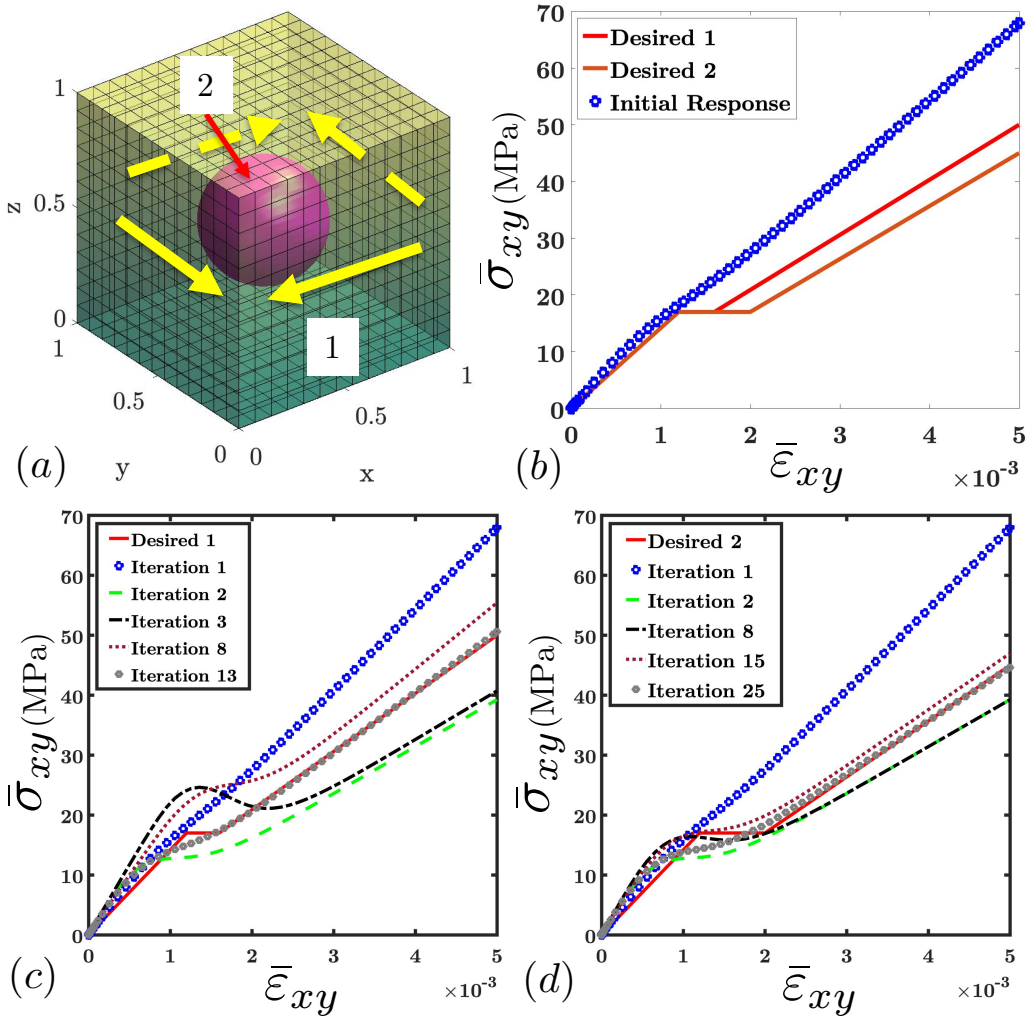

Figure 15. (a) 3D periodic unit cell with a spherical inclusion subjected to a macroscopic pure shear strain $\bar{\varepsilon}_{xy}$; (b) initial and desired stress-strain curves; (c) and (d) stress-strain curves for five selected optimization iterations, approaching the desired macroscopic responses 1 and 2, respectively.

Table IV. Optimal design variables for two different desired trilinear stress-strain curves shown in Figure 15.

	R/L	E (GPa)	Y_{in}(Pa)	p_1
Initial design	0.25	100	50	10
Desired design 1	0.35	100	10	9.99
Desired design 2	0.37	100	22.86	9.99

8. CONCLUSIONS

A gradient-based, multiscale shape optimization framework was presented for the design of materials with linear and nonlinear behavior. The multiscale method was implemented using the mathematical theory of homogenization to design the microstructure of heterogeneous materials to achieve a desired macroscopic behavior. An irreversible isotropic damage law was adopted to introduce nonlinearity into the model. This inverse homogenization problem was solved via a gradient-based shape optimization scheme. The sensitivity of this nonlinear coupled system was also provided through an analytic direct differentiation formulation that efficiently and accurately provides the gradient of the cost and constraint functions.

The numerical discretization was based on the recently introduced NURBS-based Interface-enriched Generalized Finite Element Method (NIGFEM) that is extended here to solve 3D problems. The method allows for using a fixed discretization, taking advantage of both Eulerian and Lagrangian approaches to eliminate mesh distortion issues as well as to accurately represent geometrical features.

Combining with computational homogenization and a continuous damage model, the presented optimization scheme was used to design composites microstructures with elastic and/or nonlinear response to achieve desired macroscopic behaviors.

ACKNOWLEDGEMENT

This work has been supported by the Air Force Office of Scientific Research Multidisciplinary University Research Initiative under contract # FA9550-09-1-0686. Support for M. Safdari was

provided through grant no. FA9550-12-1-0445 to the Center of Excellence on Integrated Materials Modeling (CEIMM) at Johns Hopkins University (partners JHU, UIUC, and UCSB) awarded by the AFOSR/RSL (Computational Mathematics Program, Manager Dr Sayir) and AFRL/RX (Monitors Dr Woodward and Dr Przybyla). This work was performed under the auspices of the U.S. Department of Energy by Lawrence Livermore National Laboratory under Contract DE-AC52-07NA27344. The author thanks the Livermore Graduate Scholar Program for its support. The authors also extend their gratitude to Ebrahim Maghami for assistance with some of the simulations on the high-performance computing resources at Drexel University (PROTEUS: the Drexel Cluster).

APPENDIX

A. NURBS CURVES, SURFACES, AND VOLUMES

NURBS are one of the most common methods used to represent complex curves, surfaces and volumes. A NURBS curve is built from B-splines basis functions, which are defined over a parametric space, with a set of knot vectors [87, 98, 99]. A knot vector for the 1D curve is a set of non-decreasing real numbers, ξ_i, representing coordinates (knots) in the parametric space:

$$\boldsymbol{\Xi} = \{\xi_1,\, \xi_2,\, ...,\, \xi_{l+p+1}\}\,, \tag{A.1}$$

where l is the number of B-spline basis functions and p is the polynomial order of the B-spline basis functions. Knot vectors can be presented in the normalized form,

$$\boldsymbol{\Xi} = \left\{ \overbrace{0,\, ...,\, 0}^{p+1},\, \xi_{p+2},\, ...,\, \xi_l,\, \overbrace{1,\, ...,\, 1}^{p+1} \right\}, \tag{A.2}$$

where the multiplicity adopted for the first and last knots ensures the NURBS curve passes through the end points.

The B-spline basis functions $B_{i,p}$ are defined recursively, starting with $p = 0$, as

$$B_{i,0}(\xi) = \begin{cases} 1 \text{ if } \xi_i \leq \xi < \xi_{i+1} \\ 0 \qquad \text{otherwise} \end{cases}, \tag{A.3}$$

and, for $p \geq 1$,

$$B_{i,p}(\xi) = \frac{\xi - \xi_i}{\xi_{i+p} - \xi_i} B_{i,p-1}(\xi) + \frac{\xi_{i+p+1} - \xi}{\xi_{i+p+1} - \xi_{i+1}} B_{i+1,p-1}(\xi). \tag{A.4}$$

The most notable properties of B-spline basis functions are their non-negativity, partition of unity (i.e., $\sum_{i=1}^{l} B_{i,p}(\xi) = 1$, for all ξ), and compact support. The support of $B_{i,p}$ is limited to the interval $[\xi_i, \xi_{i+p+1}]$ and in each knot span $[\xi_i, \xi_{i+1})$, there are at most $p+1$ non-zero basis functions. Moreover, they are C^{p-k} continuous at each knot with multiplicity k.

Built on B-spline basis functions, NURBS curves $\mathcal{C}$ are defined as

$$\mathcal{C} = \left\{ \xi \in [0,1] : \mathbf{X} = \mathbf{C}(\xi) = \sum_{i=1}^{l} R_{i,p}(\xi) \mathbf{P}_i \right\}, \tag{A.5}$$

where the $\mathbf{P}_i = [P_i^x \; P_i^y, P_i^z]^T$ are the control point coordinate vectors in $3D$ space, and $R_{i,p}$ are the rational B-spline basis functions, i.e., the NURBS basis functions,

$$R_{i,p}(\xi) = \frac{B_{i,p}(\xi) w_i}{\sum_{j=1}^{l} B_{j,p}(\xi) w_j}, \tag{A.6}$$

where w_i are the associated weights that are equated to one in this study.

In an analogous fashion to NURBS curves, NURBS surfaces Γ are defined from two knot vectors $\boldsymbol{\Xi} = \{\xi_1, \xi_2, ..., \xi_{l+p+1}\}$ and $\boldsymbol{\mathcal{H}} = \{\eta_1, \eta_2, ..., \eta_{m+q+1}\}$, and a bidirectional net of control points $\{\mathbf{P}_{i.j}\}$, $i = 1, 2, ..., l$, $j = 1, 2, ..., m$ as

$$\Gamma = \left\{ (\xi, \eta) \in [0,1]^2 : \mathbf{X} = \mathbf{S}(\xi, \eta) = \sum_{i=1}^{l} \sum_{j=1}^{m} R_{i.j,p.q}(\xi, \eta) \mathbf{P}_{i.j} \right\}, \tag{A.7}$$

where the basis $R_{i.j,p.q}$ functions are the tensor products of order p and q B-spline basis functions,

$$R_{i.j,p.q}(\xi,\,\eta)=\frac{B_{i,p}(\xi)\,B_{j,q}(\eta)\,w_{i.j}}{\sum\limits_{k=1}^{l}\sum\limits_{h=1}^{m}B_{k,p}(\xi)\,B_{h,q}(\eta)\,w_{k.h}}, \tag{A.8}$$

where the weights $w_{i.j}$ are again equated to one. Here, each interval $[\xi_i,\,\xi_{i+1})\times[\eta_j,\,\eta_{j+1})$ is referred to as a *knot span*. Likewise, a tridirectional net of control points $\{\mathbf{P}_{i.j.k}\}$, $i=1,\,2,\,...,\,l,\;j=1,\,2,\,...,\,m,\;k=1,\,2,\,...,\,n$ and three knot vectors $\boldsymbol{\Xi}=\{\xi_1,\,\xi_2,\,...,\,\xi_{l+p+1}\}$, $\boldsymbol{\mathcal{H}}=\{\eta_1,\,\eta_2,\,...,\,\eta_{m+q+1}\}$ and $\boldsymbol{\mathcal{Z}}=\{\zeta_1,\,\zeta_2,\,...,\,\zeta_{n+r+1}\}$, are used to define NURBS volumes Ω as

$$\Omega=\left\{(\xi,\,\eta,\,\zeta)\in[0,1]^3:\mathbf{X}=\mathbf{V}(\xi,\,\eta,\,\zeta)=\sum_{i=1}^{l}\sum_{j=1}^{m}\sum_{k=1}^{n}R_{i.j.k,p.q.r}(\xi,\,\eta,\,\zeta)\,\mathbf{P}_{i.j.k}\right\}, \tag{A.9}$$

where the basis functions

$$R_{i.j.k,p.q.r}(\xi,\,\eta)=\frac{B_{i,p}(\xi)\,B_{j,q}(\eta)\,B_{k,r}(\zeta)\,w_{i.j.k}}{\sum\limits_{e=1}^{l}\sum\limits_{g=1}^{m}\sum\limits_{h=1}^{n}B_{e,p}(\xi)\,B_{g,q}(\eta)\,B_{h,r}(\zeta)\,w_{e.g.h}}, \tag{A.10}$$

are again defined via the tensor products of order p, q and r B-spline basis functions. The basis function $R_{i.j.k,p.q.r}$ preserves all of the properties of univariate and bivariate B-spline basis functions, including compact support, non-negativity, and partition of unity. Interested readers are referred to [87, 98, 99] for more information regarding NURBS.

B. NIGFEM FORMULATION

We illustrate the NIGFEM formulation in the content of linear elastic problems. Over a 3D structural problem with domain $\Omega=\bigcup\limits_{i=1}^{N_\Omega}\Omega_i\subset\mathbb{R}^3$, $\bigcap\limits_{i=1}^{N_\Omega}\Omega_i=\emptyset$ with closure $\bar{\Omega}$, which is bounded by $\partial\Omega=\bar{\Omega}-\Omega$ with outward normal vector $\mathbf{n}$, where N_Ω is the number of subdomains $\Omega_i, i=1,2,...,N_\Omega$, over which the material is, without loss of generality, assumed to be uniform. The boundary $\partial\Omega$ is split into two complementary subsets S^t and S^u, i.e., $\partial\Omega=S^u\cup S^t$ and $S^u\cap S^t=\emptyset$, upon which

traction $\mathbf{t}$ and displacement $\mathbf{u}$ are prescribed. A body force $\mathbf{b}$ is applied throughout Ω. We assume that the material interfaces are smooth and defined by $\Gamma = \bigcup_{i=1}^{N_\Gamma} \Gamma_i \subset R^2$, where N_Γ is the number of interfaces. Without loss of generality, we also assume $\bigcap_{i=1}^{N_\Gamma} \Gamma_i = \emptyset$ (so that $N_\Gamma = N_\Omega$) and the boundary $\partial\Omega$ is fixed for the optimization and denote the normal vector on each material interface Γ_i by $\mathbf{n}_i$.

To present the finite element formulation, let us represent the NIGFEM interpolation (1) in the matrix form as follows:

$$\begin{aligned} \mathbf{u}^h(\mathbf{X}) &= \sum_{i=1}^{n_e} N_i(\mathbf{x})\mathbf{u}_i + \sum_{j=1}^{n_{\psi_j}} \sum_{k=1}^{n_{\psi_k}} \psi_{jk}(\mathbf{x})\boldsymbol{\alpha}_{jk} \\ &= \begin{bmatrix} \mathbf{N}(\mathbf{X}) & \boldsymbol{\Psi}(\mathbf{X}) \end{bmatrix} \begin{Bmatrix} \mathbf{U} \\ \mathbf{A} \end{Bmatrix}, \end{aligned} \tag{B.1}$$

where

$$\mathbf{N} = \begin{bmatrix} N_1 & 0 & 0 & N_2 & 0 & 0 & ... & N_{n_e} & 0 & 0 \\ 0 & N_1 & 0 & 0 & N_2 & 0 & ... & 0 & N_{n_e} & 0 \\ 0 & 0 & N_1 & 0 & 0 & N_2 & ... & 0 & 0 & N_{n_e} \end{bmatrix} = \mathbf{N}_e \otimes \mathbf{I}, \tag{B.2}$$

$\otimes$ is the Kronecker product[¶¶], $\mathbf{I}$ is a 3×3 identity matrix, and $\mathbf{N}_e = [N_1\ N_2\ ...N_{n_e}]$ is the vector of element shape functions. We also define

$$\begin{aligned} &\boldsymbol{\Psi} = \boldsymbol{\psi} \otimes \mathbf{I}, \\ &\mathbf{U} = \begin{bmatrix} u_1^x & u_1^y & u_1^z & u_2^x & u_2^y & u_2^z & ... & u_{n_e}^x & u_{n_e}^y & u_{n_e}^z \end{bmatrix}^T, \\ &\mathbf{A} = \begin{bmatrix} \alpha_{11}^x & \alpha_{11}^y & \alpha_{11}^z & \alpha_{12}^x & \alpha_{12}^y & \alpha_{12}^z & ... & \alpha_{n_{\psi_j} n_{\psi_k}}^x & \alpha_{n_{\psi_j} n_{\psi_k}}^y & \alpha_{n_{\psi_j} n_{\psi_k}}^z \end{bmatrix}^T, \end{aligned} \tag{B.3}$$

where $\boldsymbol{\psi} = \begin{bmatrix} \psi_{11}\ \psi_{12}\ ...\ \psi_{n_{\psi_j} n_{\psi_k}} \end{bmatrix}$.

[¶¶]The Kronecker product of two matrices A and B with $A = [a_{i,j}]$ is defined as [100]

$$A \otimes B = [a_{i,j}B].$$

For a linear elastic problem, the discretized equilibrium equation is

$$\mathbb{K}\mathbb{U} = \mathbb{F}, \tag{B.4}$$

where $\mathbb{U}$, $\mathbb{F}$, and $\mathbb{K}$ denote the global displacement vector, global force vector, and global stiffness matrix, respectively. As usual, $\mathbb{K}$ is assembled from the element Ω_e stiffness matrices $\mathbf{K}^e$,

$$\mathbf{K}^e = \int_{\Omega_e} \mathbb{B}^T(\mathbf{X})\, \mathbb{D}(\mathbf{X})\, \mathbb{B}(\mathbf{X})\; d\Omega, \tag{B.5}$$

where $\mathbb{D}$ is the constitutive matrix for a linear elastic material. The strain displacement matrix

$$\mathbb{B}(\mathbf{X}) = \begin{bmatrix} \mathbf{B}_N(\mathbf{X}) & \mathbf{B}_\psi(\mathbf{X}) \end{bmatrix} \tag{B.6}$$

is partitioned such that

$$\mathbf{B}_N(\mathbf{X}) = \begin{bmatrix} \frac{\partial N_1}{\partial x} & 0 & 0 & \frac{\partial N_2}{\partial x} & 0 & 0 & \dots & \frac{\partial N_{n_e}}{\partial x} & 0 & 0 \\ 0 & \frac{\partial N_1}{\partial y} & 0 & 0 & \frac{\partial N_2}{\partial y} & 0 & \dots & 0 & \frac{\partial N_{n_e}}{\partial y} & 0 \\ 0 & 0 & \frac{\partial N_1}{\partial z} & 0 & 0 & \frac{\partial N_2}{\partial z} & \dots & 0 & 0 & \frac{\partial N_{n_e}}{\partial z} \\ \frac{\partial N_1}{\partial y} & \frac{\partial N_1}{\partial x} & 0 & \frac{\partial N_2}{\partial y} & \frac{\partial N_2}{\partial x} & 0 & \dots & \frac{\partial N_{n_e}}{\partial y} & \frac{\partial N_{n_e}}{\partial x} & 0 \\ 0 & \frac{\partial N_1}{\partial z} & \frac{\partial N_1}{\partial y} & 0 & \frac{\partial N_2}{\partial z} & \frac{\partial N_2}{\partial y} & \dots & 0 & \frac{\partial N_{n_e}}{\partial z} & \frac{\partial N_{n_e}}{\partial y} \\ \frac{\partial N_1}{\partial z} & 0 & \frac{\partial N_1}{\partial x} & \frac{\partial N_2}{\partial z} & 0 & \frac{\partial N_2}{\partial x} & \dots & \frac{\partial N_{n_e}}{\partial z} & 0 & \frac{\partial N_{n_e}}{\partial x} \end{bmatrix},$$

$$\mathbf{B}_\psi(\mathbf{X}) = \begin{bmatrix} \frac{\partial \psi_{11}}{\partial x} & 0 & 0 & \frac{\partial \psi_{12}}{\partial x} & 0 & 0 & \dots & \frac{\partial \psi_{n_{\psi_j} n_{\psi_k}}}{\partial x} & 0 & 0 \\ 0 & \frac{\partial \psi_{11}}{\partial y} & 0 & 0 & \frac{\partial \psi_{12}}{\partial y} & 0 & \dots & 0 & \frac{\partial \psi_{n_{\psi_j} n_{\psi_k}}}{\partial y} & 0 \\ 0 & 0 & \frac{\partial \psi_{11}}{\partial z} & 0 & 0 & \frac{\partial \psi_{12}}{\partial z} & \dots & 0 & 0 & \frac{\partial \psi_{n_{\psi_j} n_{\psi_k}}}{\partial z} \\ \frac{\partial \psi_{11}}{\partial y} & \frac{\partial \psi_{11}}{\partial x} & 0 & \frac{\partial \psi_{12}}{\partial y} & \frac{\partial \psi_{12}}{\partial x} & 0 & \dots & \frac{\partial \psi_{n_{\psi_j} n_{\psi_k}}}{\partial y} & \frac{\partial \psi_{n_{\psi_j} n_{\psi_k}}}{\partial x} & 0 \\ 0 & \frac{\partial \psi_{11}}{\partial z} & \frac{\partial \psi_{11}}{\partial y} & 0 & \frac{\partial \psi_{12}}{\partial z} & \frac{\partial \psi_{12}}{\partial y} & \dots & 0 & \frac{\partial \psi_{n_{\psi_j} n_{\psi_k}}}{\partial z} & \frac{\partial \psi_{n_{\psi_j} n_{\psi_k}}}{\partial y} \\ \frac{\partial \psi_{11}}{\partial z} & 0 & \frac{\partial \psi_{11}}{\partial x} & \frac{\partial \psi_{12}}{\partial z} & 0 & \frac{\partial \psi_{12}}{\partial x} & \dots & \frac{\partial \psi_{n_{\psi_j} n_{\psi_k}}}{\partial z} & 0 & \frac{\partial \psi_{n_{\psi_j} n_{\psi_k}}}{\partial x} \end{bmatrix}. \tag{B.7}$$

By substituting (B.6) into (B.5), we have

$$\mathbf{K}^e = \begin{bmatrix} \mathbf{K}^e_{uu} & \mathbf{K}^e_{u\alpha} \\ (\mathbf{K}^e_{u\alpha})^T & \mathbf{K}^e_{\alpha\alpha} \end{bmatrix}, \tag{B.8}$$

where

$$\begin{aligned} \mathbf{K}^e_{uu} &= \sum_{i=1}^{m_s} \int_{\Omega_e^{(i)}} \mathbf{B}_N^T(\mathbf{X})\, \mathbb{D}(\mathbf{X})\, \mathbf{B}_N(\mathbf{X})\, d\Omega, \\ \mathbf{K}^e_{u\alpha} &= \sum_{i=1}^{m_s} \int_{\Omega_e^{(i)}} \mathbf{B}_N^T(\mathbf{X})\, \mathbb{D}(\mathbf{X})\, \mathbf{B}_\psi(\mathbf{X})\, d\Omega, \\ \mathbf{K}^e_{\alpha\alpha} &= \sum_{i=1}^{m_s} \int_{\Omega_e^{(i)}} \mathbf{B}_\psi^T(\mathbf{X})\, \mathbb{D}(\mathbf{X})\, \mathbf{B}_\psi(\mathbf{X})\, d\Omega, \end{aligned} \tag{B.9}$$

and m_s is the number of subdomains in an enriched element. The above holds for the enriched elements. For all the other elements, $\mathbf{B}_\psi = 0$, and the element stiffness matrix takes the usual form.

Similarly, the global nodal force vector $\mathbb{F}$ in (B.4) is assembled from the element nodal force vector $\mathbf{F}^e$,

$$\mathbf{F}^e = \int_{\Omega_e} \mathbb{N}^T(\mathbf{X})\, \mathbf{b}(\mathbf{X})\, d\Omega + \int_{\Gamma_e \cap S^t} \mathbb{N}^T(\mathbf{X})\, \mathbf{t}(\mathbf{X})\, d\Gamma, \tag{B.10}$$

where $\mathbb{N}$ is the element shape function vector, given by

$$\mathbb{N}(\mathbf{X}) = \begin{bmatrix} \mathbf{N}(\mathbf{X}) & \mathbf{\Psi}(\mathbf{X}) \end{bmatrix}. \tag{B.11}$$

Substituting (B.11) into (B.10) leads to

$$\mathbf{F}^e = \begin{bmatrix} \mathbf{F}^e_u \\ \mathbf{F}^e_\alpha \end{bmatrix}, \tag{B.12}$$

where

$$\mathbf{F}_u^e = \sum_{i=1}^{m_s} \left[\int_{\Omega_e^{(i)}} \mathbf{N}^T(\mathbf{X})\, \mathbf{b}(\mathbf{X})\, d\Omega + \int_{\Gamma_e^{(i)} \cap S^t} \mathbf{N}^T(\mathbf{X})\, \mathbf{t}(\mathbf{X})\, d\Gamma \right],$$
$$\mathbf{F}_\alpha^e = \sum_{i=1}^{m_s} \left[\int_{\Omega_e^{(i)}} \mathbf{\Psi}^T(\mathbf{X})\, \mathbf{b}(\mathbf{X})\, d\Omega + \int_{\Gamma_e^{(i)} \cap S^t} \mathbf{\Psi}^T(\mathbf{X})\, \mathbf{t}(\mathbf{X})\, d\Gamma \right]. \tag{B.13}$$

As with the element stiffness matrix, $\mathbf{F}_\alpha^e \neq 0$ only for the enriched elements. To evaluate the integrals appearing over the enriched element subdomains $\Omega_e^{(i)}$ in (B.9) and (B.13) special care must be taken. We perform these integrations by Gaussian quadrature using a span-wise mapping (SWM) in which the element sub-domains serve as integration elements. Further details about NIGFEM integration and quadrature scheme are provided in [72,74,75]. It is worth mentioning that the SWM affects the sensitivity analysis.

C. INTRODUCING THE CONTROL POINTS ON SUB-INTERFACE Γ_e^h

To discuss how sixteen control points of the sub-interface Γ_e^h (illustrated in Figure 2) are defined, consider Figure C16. The four control points $\{\mathbf{P}_{i.1.0}\}$, $i = 1, ..., 4$ (shown by red cubes) that define the boundary NURBS curve C_1^e, are on the element top face. To determine their precise location, we first find the intersections between the material interface Γ and the element edges. This step is readily done to obtain the intersection points A and E (shown by the blue triangles). In the next step, we draw two lines on the top face that are perpendicular to the line segment AE and that divide it evenly (shown by the green lines, marked with $L_i, i = 1, 2$). Please refer to Appendix D for more details on constructing the NURBS equations of the lines L_i. The intersection of these two lines with the material interface Γ defines points B and D (depicted by the green circles). We finally use the global curve interpolation algorithm to construct the NURBS curve C_1^e that passes through points A, B, D, and E [87]. In this approach, we use a chord length technique (see the Appendix E) to assign a parameter value, β_i, to each intersection point and select an appropriate knot vector

560 $\mathcal{B} = \{\beta_1 = \beta_A = 0, \beta_2 = \beta_B, \beta_3 = \beta_D, \beta_4 = \beta_E = 1\}$. We then solve linear equations

$$\mathbf{Q}_j = \mathbf{C}_1^e(\beta_j) = \sum_{i=1}^{NCP=4} R_i(\beta_j)\,\mathbf{P}_{i.1.0} \tag{C.1}$$

for the control point coordinates $\{\mathbf{P}_{i.1.0}\}$, $i = 1, ..., 4$, where $\mathbf{Q}_j$, $j = 1, ..., 4$, denotes the coordinates $\mathbf{A}$, $\mathbf{B}$, $\mathbf{D}$, and $\mathbf{E}$ of the intersection points A, B, D, and E, $NCP = 4$ denotes the number of control points of C_1^e, and R_i are the NURBS basis functions defined in A.6. We can find the remaining control points of the sub-interface Γ_e^h (i.e., $\{\mathbf{P}_{i.j.0}\}$, $i = 1, ..., 4, j = 2, ..., 4$) in

565 a similar manner.

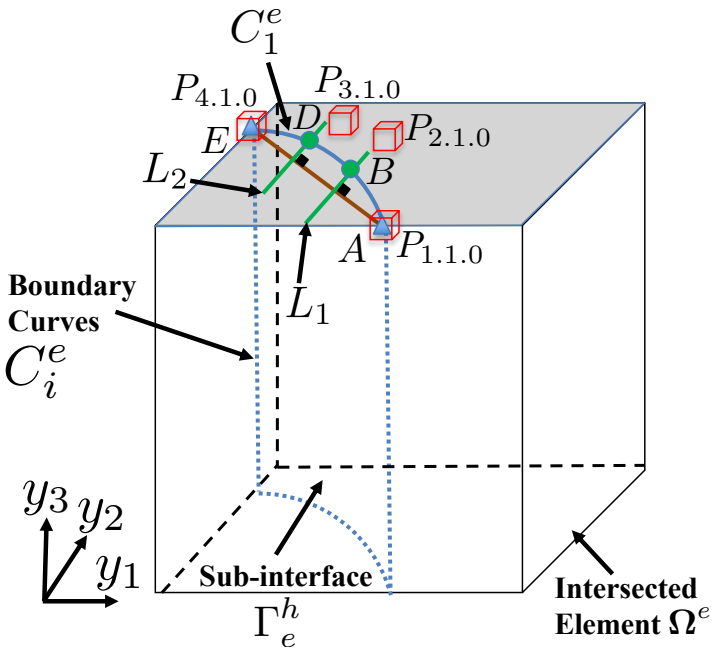

Figure C16. Procedure to find the control point coordinates of the sub-interface Γ_e^h that are used to define the boundary curves C_i^e. The control points are shown with the red cubes and the intersection points are depicted by the blue triangles and green circles.

D. CONSTRUCTING THE NURBS LINE L_i

Figure D17 redraws Figure C16 in $y_1 - y_2$ plane. As explained in Appendix C, the lines L_1 and L_2 are perpendicular to the line segment AE and divide it evenly. The NURBS equation of line L_1 has

the form

$$\mathbf{L}_1(\gamma_B) = \sum_{i=1}^{2} R_i(\gamma_B)\,\mathbf{P}_{L_i}, \tag{D.1}$$

where R_i are the NURBS basis functions introduced in A.6 and $\mathbf{P}_{L_i}$ are the control point coordinates of line L_1 (shown by green (+)) defined as

$$\begin{cases} \mathbf{P}_{L_1} = \mathbf{O} - \mathbf{n}_1 \\ \mathbf{P}_{L_2} = \mathbf{O} + \mathbf{n}_1 \end{cases}, \tag{D.2}$$

where $\mathbf{O} = \mathbf{A} + \mathbf{l}$ with $\mathbf{l} = \dfrac{\mathbf{E} - \mathbf{A}}{3}$ (as shown in Figure D17) and

$$\mathbf{n}_1 = h\frac{\mathbf{e}_3 \times \mathbf{l}}{\|\mathbf{e}_3 \times \mathbf{l}\|}. \tag{D.3}$$

In (D.3), $\mathbf{e}_i$ is the basis vector in the y_i direction and the constant h is half the diagonal length of the element face.

As seen in Appendix F, to compute the design velocity of intersection point B using (F.6) we need to obtain the velocity of $\mathbf{P}_{L_i}$ (i.e. the sensitivity $\dfrac{\partial \mathbf{P}_{L_i}}{\partial d_q}$). To this end, we differentiate (D.2) with respect to the geometrical design parameter d_q to obtain

$$\frac{\partial \mathbf{P}_{L_i}}{\partial d_q} = \frac{\partial \mathbf{O}}{\partial d_q} \pm \frac{\partial \mathbf{n}_1}{\partial d_q}, \tag{D.4}$$

where

$$\begin{aligned} \frac{\partial \mathbf{O}}{\partial d_q} &= \frac{\partial \mathbf{A}}{\partial d_q} + \frac{\partial \mathbf{l}}{\partial d_q} \\ &= \frac{\partial \mathbf{A}}{\partial d_q} + \frac{1}{3}\frac{\partial (\mathbf{E} - \mathbf{A})}{\partial d_q}, \end{aligned} \tag{D.5}$$

and

$$\frac{\partial \mathbf{n}_1}{\partial d_q} = \frac{\left[\left(\mathbf{e}_3 \times \frac{\partial \mathbf{l}}{\partial d_q}\right)\|\mathbf{e}_3 \times \mathbf{l}\|\,h - (\mathbf{e}_3 \times \mathbf{l}) \times \left(\mathbf{n}_1 \cdot \left(\mathbf{e}_3 \times \frac{\partial \mathbf{l}}{\partial d_q}\right)\right)\right]}{\|\mathbf{e}_3 \times \mathbf{l}\|^2}. \tag{D.6}$$

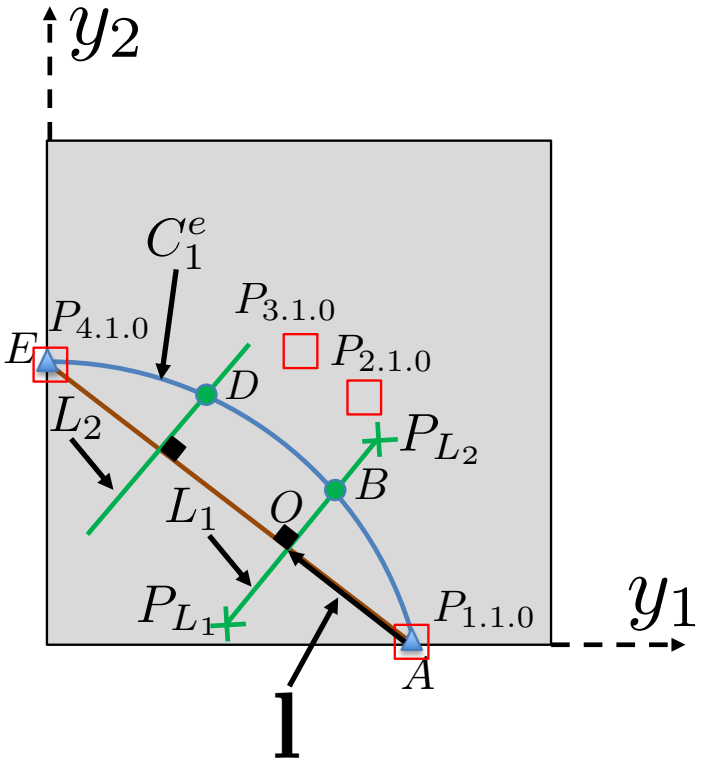

Figure D17. Construction of NURBS curve for lines L_1 and L_2.

The sensitivities $\frac{\partial \mathbf{A}}{\partial d_q}$ and $\frac{\partial \mathbf{E}}{\partial d_q}$ appearing in (D.5) are computed using (F.2).

E. CHORD LENGTH TECHNIQUE

To construct the NURBS curve C_i^e that interpolates a given set of points $Q_j, j = 1, ..., NCP = 4$ (e.g., the intersection points A, B, D, and E, illustrated in Figure C16), we employ the global curve interpolation method [87]. In this approach, we assign a parameter value, β_j, to each point by using the chord length technique presented in [87]. We require $\beta \in [0, 1]$ and select the knot vector $\boldsymbol{\mathcal{B}} = \{\beta_1 = \beta_A = 0, \beta_2 = \beta_B, \beta_3 = \beta_D, \beta_4 = \beta_E = 1\}$, where $\beta_2 = \beta_B$ and $\beta_3 = \beta_D$ are computed from

$$\beta_j = \beta_{j-1} + \frac{|\mathbf{Q}_j - \mathbf{Q}_{j-1}|}{L}, \quad j = 2, 3, \tag{E.1}$$

where $\mathbf{Q}_i$ is the coordinate vector of the point Q_i and

$$L = \sum_{j=2}^{4} |\mathbf{Q}_j - \mathbf{Q}_{j-1}| \,. \tag{E.2}$$

To perform the sensitivity analysis, we also need to have the sensitivity of the parameter β_j with respect to design parameter d_i, i.e., $\dfrac{\partial \beta_j}{\partial d_i}$. Since we assign $\beta_1 = \beta_A = 0$ and $\beta_4 = \beta_E = 1$, we have

$$\frac{\partial \beta_1}{\partial d_i} = \frac{\partial \beta_A}{\partial d_i} = 0, \text{ and } \frac{\partial \beta_4}{\partial d_i} = \frac{\partial \beta_E}{\partial d_i} = 0. \tag{E.3}$$

Taking derivative of (E.1) with respect to design parameter d_i, we obtain

$$\frac{\partial \beta}{\partial d_i}\Big|_{\beta=\beta_j} = \frac{\partial \beta}{\partial d_i}\Big|_{\beta=\beta_{j-1}} + \frac{\frac{\partial |\mathbf{Q}_j - \mathbf{Q}_{j-1}|}{\partial d_i} L - |\mathbf{Q}_j - \mathbf{Q}_{j-1}| \frac{\partial L}{\partial d_i}}{L^2}, \quad j = 2, 3, \tag{E.4}$$

where

$$\frac{\partial L}{\partial d_i} = \sum_{j=2}^{4} \frac{\partial \, |\mathbf{Q}_j - \mathbf{Q}_{j-1}|}{\partial d_i}. \tag{E.5}$$

F. DESIGN VELOCITY OF THE ENRICHED CONTROL POINTS

In this section, we compute the shape velocity associated with the control points of an integration element. Note that all the control point velocities for an enriched element, except those of the enriched control points (i.e., $\{\mathbf{P}_{j.k.0}\}$, $j, k = 1, ..., m = n = 4$ on the sub-interface Γ_e^h in Figure 2), are zero. Referring to Figure C16, we evaluate the velocity of the control points $\{\mathbf{P}_{j.1.0}\}$, $j = 1, ..., m = 4$ by first obtaining the velocity of the intersection point coordinates $\mathbf{A}, \mathbf{B}, \mathbf{D}$, and $\mathbf{E}$. Let us derive the design velocity field for $\mathbf{A}$ that satisfies (2), that is,

$$\mathbf{A} = \mathbf{S}\left(\xi_A, \eta_A\right) = \sum_{i=1}^{l} \sum_{j=1}^{m} R_{i.j}\left(\xi_A, \, \eta_A\right) \mathbf{P}_{i.j}, \tag{F.1}$$

where $(\xi_A, \, \eta_A)$ denotes the parametric coordinates (knot values), and $\mathbf{P}_{i.j}$ are the control point coordinates that define the material interface Γ, presented in (A.7). Assuming that d_q is a geometrical

design variable and differentiating (F.1) gives

$$
\begin{aligned}
{}^{A}\mathbb{V}_q = \frac{\partial \mathbf{S}\left(\xi_A, \eta_A\right)}{\partial d_q} = & \left(\sum_{i=1}^{l}\sum_{j=1}^{m}\frac{\partial R_{i.j}\left(\xi_A,\, \eta_A\right)}{\partial \xi}\mathbf{P}_{i.j}\right)\frac{\partial \xi_A}{\partial d_q} \\
& + \left(\sum_{i=1}^{l}\sum_{j=1}^{m}\frac{\partial R_{i.j}\left(\xi_A,\, \eta_A\right)}{\partial \eta}\mathbf{P}_{i.j}\right)\frac{\partial \eta_A}{\partial d_q} + \sum_{i=1}^{l}\sum_{j=1}^{m}R_{i.j}\left(\xi_A,\, \eta_A\right)\frac{\partial \mathbf{P}_{i.j}}{\partial d_q}
\end{aligned}
\tag{F.2}
$$

where the vector ${}^{A}\mathbb{V}_q$ denotes the design velocity of intersection point A. To compute the velocity ${}^{A}\mathbb{V}_q$, we must first evalute the unknown sensitivities $\frac{\partial \xi_A}{\partial d_q}$ and $\frac{\partial \eta_A}{\partial d_q}$. Referring to Figure C16, we see that the intersection point A is always located on the top face and on an element edge that is parallel to $\mathbf{e}_1$. Due to this fact, $\mathbf{e}_2$ and $\mathbf{e}_3$ components of ${}^{A}\mathbb{V}_q$ are zero . Equating these components ${}^{A}\mathbb{V}_q$ to zero results in a linear equation that we use to compute $\frac{\partial \xi_A}{\partial d_q}$ and $\frac{\partial \eta_A}{\partial d_q}$ and subsequently ${}^{A}\mathbb{V}_q$ via (F.2). The same approach is used to compute the design velocity field for intersection point coordinate $\mathbf{E}$, i.e. ${}^{E}\mathbb{V}_q$.

In the next step, we compute the design velocity of intersection point coordinates $\mathbf{B}$ and $\mathbf{D}$. Let us start with the point B. As shown in Figure C16, the intersection point B (i.e., $\Gamma \cap L_1$) satisfies

$$
\mathbf{S}\left(\xi_B,\, \eta_B\right) - \mathbf{L}_1\left(\gamma_B\right) = \mathbf{0}, \tag{F.3}
$$

where $(\xi_A,\, \eta_A)$ and γ_B are the parametric coordinates (knot values) of the intersection point B on the material interface Γ and the line L_1, respectively, and $\mathbf{S}$ and $\mathbf{L}$ are defined by (F.1) and (D.1). To compute ${}^{B}\mathbb{V}_q$ we first differentiate (F.3) to obtain

$$
\begin{aligned}
& \left(\sum_{i=1}^{l}\sum_{j=1}^{m}\frac{\partial R_{i.j}\left(\xi_B,\, \eta_B\right)}{\partial \xi}\mathbf{P}_{i.j}\right)\frac{\partial \xi_B}{\partial d_q} + \left(\sum_{i=1}^{l}\sum_{j=1}^{m}\frac{\partial R_{i.j}\left(\xi_B,\, \eta_B\right)}{\partial \eta}\mathbf{P}_{i.j}\right)\frac{\partial \eta_B}{\partial d_q} \\
& + \sum_{i=1}^{l}\sum_{j=1}^{m}R_{i.j}\left(\xi_B,\, \eta_B\right)\frac{\partial \mathbf{P}_{i.j}}{\partial d_q} - \left\{\left(\sum_{i=1}^{r}\frac{\partial R_i\left(\gamma_B\right)}{\partial \gamma}\mathbf{P}_{L_i}\right)\frac{\partial \gamma_B}{\partial d_q} + \sum_{i=1}^{r}R_i\left(\gamma_B\right)\frac{\partial \mathbf{P}_{L_i}}{\partial d_q}\right\} = 0
\end{aligned}
\tag{F.4}
$$

Rearranging (F.4) in a matrix form yields a linear equation which we solve to evaluate $\frac{\partial \xi_B}{\partial d_q}$, $\frac{\partial \eta_B}{\partial d_q}$, and $\frac{\partial \gamma_B}{\partial d_q}$, i.e.

$$\begin{bmatrix} \sum_{i=1}^{l}\sum_{j=1}^{m} \frac{\partial R_{i.j}(\xi_B,\eta_B)}{\partial \xi}\mathbf{P}_{i.j} & \sum_{i=1}^{l}\sum_{j=1}^{m} \frac{\partial R_{i.j}(\xi_B,\eta_B)}{\partial \eta}\mathbf{P}_{i.j} & -\sum_{i=1}^{r} \frac{\partial R_i(\gamma_B)}{\partial \gamma}\mathbf{P}_{L_i} \end{bmatrix} \times \\ \begin{Bmatrix} \frac{\partial \xi_B}{\partial d_q} \\ \frac{\partial \eta_B}{\partial d_q} \\ \frac{\partial \gamma_B}{\partial d_q} \end{Bmatrix} = \begin{bmatrix} \sum_{i=1}^{r} R_i(\gamma_B)\frac{\partial \mathbf{P}_{L_i}}{\partial d_q} - \sum_{i=1}^{l}\sum_{j=1}^{m} R_{i.j}(\xi_B,\eta_B)\frac{\partial \mathbf{P}_{i.j}}{\partial d_q} \end{bmatrix}, \tag{F.5}$$

where the computation of $\frac{\partial \mathbf{P}_{L_i}}{\partial d_q}$ is presented in the Appendix D. Subsequently, we compute

$$\begin{aligned} {}^{B}\mathbb{V}_q &= \frac{\partial \mathbf{L}(\gamma_B)}{\partial d_q} \\ &= \left(\sum_{i=1}^{r} \frac{\partial R_i(\gamma_B)}{\partial \gamma}\mathbf{P}_{L_i}\right)\frac{\partial \gamma_B}{\partial d_q} + \sum_{i=1}^{r} R_i(\gamma_B)\frac{\partial \mathbf{P}_{L_i}}{\partial d_q}. \end{aligned} \tag{F.6}$$

615 or alternatively as

$$\begin{aligned} {}^{B}\mathbb{V}_q &= \frac{\partial \mathbf{S}(\xi_B,\eta_B)}{\partial d_q} \\ &= \left(\sum_{i=1}^{l}\sum_{j=1}^{m} \frac{\partial R_{i.j}(\xi_B,\eta_B)}{\partial \xi}\mathbf{P}_{i.j}\right)\frac{\partial \xi_B}{\partial d_q} + \left(\sum_{i=1}^{l}\sum_{j=1}^{m} \frac{\partial R_{i.j}(\xi_B,\eta_B)}{\partial \eta}\mathbf{P}_{i.j}\right)\frac{\partial \eta_B}{\partial d_q} \\ &+ \sum_{i=1}^{l}\sum_{j=1}^{m} R_{i.j}(\xi_B,\eta_B)\frac{\partial \mathbf{P}_{i.j}}{\partial d_q}. \end{aligned} \tag{F.7}$$

In the same way, we compute the design velocity field of the intersection point D.

Having the design velocities ${}^{A}\mathbb{V}_q$, ${}^{B}\mathbb{V}_q$, ${}^{D}\mathbb{V}_q$ and ${}^{E}\mathbb{V}_q$, we can evaluate the velocities of control points $\{\mathbf{P}_{j.1.0}\}$, $j = 1, ..., m = 4$. Referring to Figure C16 we see that the control points $\mathbf{P}_{1.1.0}$ and $\mathbf{P}_{4.1.0}$ coincide with points A and E, therefore,

$$\begin{aligned} \frac{\partial \mathbf{P}_{1.1.0}}{\partial d_q} &= {}^{A}\mathbb{V}_q \\ \frac{\partial \mathbf{P}_{4.1.0}}{\partial d_q} &= {}^{E}\mathbb{V}_q \end{aligned} \tag{F.8}$$

To compute the design velocity of the control points $\mathbf{P}_{2.1.0}$ and $\mathbf{P}_{3.1.0}$, we differentiate the NURBS curve (C.1) at the parameter values $\beta = \beta_B$ and $\beta = \beta_D$ to obtain

$$\begin{aligned} {}^{B}\mathbb{V}_q &= \frac{\partial \mathbf{C}(\beta_B)}{\partial d_q} = \left(\sum_{i=1}^{NCP=4} \frac{\partial R_i(\beta_B)}{\partial \beta} \mathbf{P}_{i.1.0} \right) \frac{\partial \beta_B}{\partial d_q} + \sum_{i=1}^{NCP=4} R_i(\beta_B) \frac{\partial \mathbf{P}_{i.1.0}}{\partial d_q} \\ {}^{D}\mathbb{V}_q &= \frac{\partial \mathbf{C}(\beta_D)}{\partial d_q} = \left(\sum_{i=1}^{NCP=4} \frac{\partial R_i(\beta_D)}{\partial \beta} \mathbf{P}_{i.1.0} \right) \frac{\partial \beta_D}{\partial d_q} + \sum_{i=1}^{NCP=4} R_i(\beta_D) \frac{\partial \mathbf{P}_{i.1.0}}{\partial d_q} \end{aligned} . \tag{F.9}$$

where ${}^{B}\mathbb{V}_q$ and ${}^{D}\mathbb{V}_q$ are obtained from (F.6) and $\frac{\partial \beta_B}{\partial d_q}$ and $\frac{\partial \beta_D}{\partial d_q}$ from (E.4). The linear equation (F.9) is trivially solved for the sensitivities $\frac{\partial \mathbf{P}_{2.1.0}}{\partial d_q}$ and $\frac{\partial \mathbf{P}_{3.1.0}}{\partial d_q}$. This completes the evaluation of control point design velocities.

G. SENSITIVITY OF THE RESIDUALS WITH RESPECT TO MATERIAL PARAMETERS

If d_i is parameter that describes $\mathbf{D}_0$, the derivative $\frac{\partial^n \mathbf{R}_{gp}}{\partial d_i}$ of the element Gauss point equilibrium and damage evolution residuals are computed as

$$\frac{\partial^n \mathbf{R}_{gp}}{\partial d_i} = \mathbb{B}^T \left(1 - {}^{n}\omega\right) \frac{\partial \mathbf{D}_0}{\partial d_i} \left(\bar{\boldsymbol{\varepsilon}} + \mathbb{B}^n \tilde{\mathbf{U}}^e \right), \tag{G.1}$$

$$\frac{\partial^n H_{gp}}{\partial d_i} = \begin{cases} \dfrac{\Delta t\, \mu}{1 + \Delta t\, \mu} \dfrac{\partial G}{\partial^n \bar{Y}} \dfrac{1}{2} \left(\bar{\boldsymbol{\varepsilon}} + \mathbb{B}^n \tilde{\mathbf{U}}^e \right)^T \dfrac{\partial \mathbf{D}_0}{\partial d_i} \left(\bar{\boldsymbol{\varepsilon}} + \mathbb{B}^n \tilde{\mathbf{U}}^e \right) & \text{if } g \geq 0 \\ 0 & \text{if } g < 0 \end{cases} . \tag{G.2}$$

For the damage material parameters Y_{in} and p_1, $\frac{\partial^n \mathbf{R}_{gp}}{\partial d_i} = 0$ and and for $d_q = Y_{in}$

$$\frac{\partial^n H_{gp}}{\partial d_q} = \begin{cases} \dfrac{\Delta t\, \mu}{1 + \Delta t\, \mu} \left[p_2 \left(\dfrac{\bar{Y} - Y_{in}}{p_1 Y_{in}} \right)^{p_2 - 1} \dfrac{-p_1 Y_{in} - p_1 \left(\bar{Y} - Y_{in} \right)}{\left(p_1 Y_{in} \right)^2} \left(exp \left[- \left(\dfrac{\bar{Y} - Y_{in}}{p_1 Y_{in}} \right)^{p_2} \right] \right) \right] & \text{if } g \geq 0 \\ 0 & \text{if } g < 0 \end{cases} , \tag{G.3}$$

whereas for $d_q = p_1$

$$\frac{\partial^n H_{gp}}{\partial d_q} = \begin{cases} \dfrac{\Delta t\,\mu}{1+\Delta t\,\mu}\left[p_2\left(\dfrac{\bar{Y}-Y_{in}}{p_1 Y_{in}}\right)^{p_2-1}\dfrac{-Y_{in}\left(\bar{Y}-Y_{in}\right)}{\left(p_1 Y_{in}\right)^2}\left(exp\left[-\left(\dfrac{\bar{Y}-Y_{in}}{p_1 Y_{in}}\right)^{p_2}\right]\right)\right] & \text{if } g \geq 0 \\ 0 & \text{if } g < 0 \end{cases} . \tag{G.4}$$

It is worth mentioning that we need to compute $\dfrac{\partial^n \mathbf{R}_{gp}}{\partial d_i}$ for both the enriched and regular elements.

DATA AVAILABILITY STATEMENT

Data sharing not applicable to this article as no datasets were generated or analyzed during the current study.

REFERENCES

1. Hashin Z, Shtrikman S. A variational approach to the theory of the effective magnetic permeability of multiphase materials. *Journal of Applied Physics* 1962; **33**:3125–3131.
2. Milton GW. On characterizing the set of possible effective tensors of composites: The variational method and the translation method. *Communications on Pure and Applied Mathematics* 1990; **43**(1):63–125, doi: 10.1002/cpa.3160430104. URL http://dx.doi.org/10.1002/cpa.3160430104.
3. Torquato S. *Random heterogeneous materials: microstructure and macroscopic properties*, vol. 16. Springer Science & Business Media, 2013.
4. Lee SB, Kim IC, Miller CA, Torquato S. Random-walk simulation of diffusion-controlled processes among static traps. *Physical Review B* Jun 1989; **39**:11 833–11 839, doi:10.1103/PhysRevB.39.11833. URL http://link.aps.org/doi/10.1103/PhysRevB.39.11833.
5. Eyre DJ, Milton GW. A fast numerical scheme for computing the response of composites using grid refinement. *The European Physical Journal - Applied Physics* 4 1999; **6**:41–47, doi:10.1051/epjap:1999150. URL http://www.epjap.org/action/article_S1286004299001500.
6. Martys NS, Hagedorn JG. Multiscale modeling of fluid transport in heterogeneous materials using discrete boltzmann methods. *Materials and Structures* 2002; **35**(10):650–658, doi:10.1007/BF02480358. URL http://dx.doi.org/10.1007/BF02480358.

7. Torquato S. Optimal design of heterogeneous materials. *Annual Review of Materials Research* 2014/08/22 2010; **40**(1):101–129.
8. Sigmund O. Materials with prescribed constitutive parameters: An inverse homogenization problem. *International Journal of Solids and Structures* 9 1994; **31**(17):2313–2329.
9. Sigmund O. Tailoring materials with prescribed elastic properties. *Mechanics of Materials* 6 1995; **20**(4):351–368.
10. Sigmund O, Torquato S. Design of materials with extreme thermal expansion using a three-phase topology optimization method. *Smart Structures and Materials 1997: Smart Materials Technologies*, vol. 3040, Huston WCSIAADR (ed.), San Diego, CA, 1997; 52–60.
11. Hyun S, Torquato S. Designing composite microstructures with targeted properties. *Journal of Materials Research* 2001; **16**(01):280–285.
12. Takezawa A, Kobashi M. Design methodology for porous composites with tunable thermal expansion produced by multi-material topology optimization and additive manufacturing. *Composites Part B: Engineering* 2017; **131**:21 – 29, doi:https://doi.org/10.1016/j.compositesb.2017.07.054. URL http://www.sciencedirect.com/science/article/pii/S1359836817307291.
13. Li H, Luo Z, Gao L, Walker P. Topology optimization for functionally graded cellular composites with metamaterials by level sets. *Computer Methods in Applied Mechanics and Engineering* 2018; **328**:340 – 364, doi:https://doi.org/10.1016/j.cma.2017.09.008. URL http://www.sciencedirect.com/science/article/pii/S0045782516310106.
14. Guest JK, Prévost JH. Optimizing multifunctional materials: Design of microstructures for maximized stiffness and fluid permeability. *International Journal of Solids and Structures* 11 2006; **43**(22–23):7028–7047.
15. Andreassen E, Lazarov BS, Sigmund O. Design of manufacturable 3d extremal elastic microstructure. *Mechanics of Materials* 2014; **69**(1):1 – 10, doi:https://doi.org/10.1016/j.mechmat.2013.09.018. URL http://www.sciencedirect.com/science/article/pii/S0167663613002093.
16. Wang Y, Luo Z, Zhang N, Kang Z. Topological shape optimization of microstructural metamaterials using a level set method. *Computational Materials Science* 2014; **87**:178 – 186, doi:https://doi.org/10.1016/j.commatsci.2014.02.006. URL http://www.sciencedirect.com/science/article/pii/S0927025614000883.
17. Wu J, Luo Z, Li H, Zhang N. Level-set topology optimization for mechanical metamaterials under hybrid uncertainties. *Computer Methods in Applied Mechanics and Engineering* 2017; **319**:414 – 441, doi:https://doi.org/10.1016/j.cma.2017.03.002. URL http://www.sciencedirect.com/science/article/pii/S0045782516310088.
18. Watts S, Tortorelli DA. A geometric projection method for designing three-dimensional open lattices with inverse homogenization. *International Journal for Numerical Methods in Engineering* 2017; **112**(11):1564–1588, doi:10.1002/nme.5569. URL https://onlinelibrary.wiley.com/doi/abs/10.1002/nme.5569.
19. Torquato S, Hyun S, Donev A. Optimal design of manufacturable three-dimensional composites with multifunctional characteristics. *Journal of Applied Physics* 2003; **94**(9):5748–5755.

20. Kursa M, Kowalczyk-Gajewska K, Petryk H. Multi-objective optimization of thermo-mechanical properties of metal–ceramic composites. *Composites Part B: Engineering* 4 2014; **60**:586–596.

21. Wang Y, Gao J, Luo Z, Brown T, Zhang N. Level-set topology optimization for multimaterial and multifunctional mechanical metamaterials. *Engineering Optimization* 2017; **49**(1):22–42, doi:10.1080/0305215X.2016.1164853. URL https://doi.org/10.1080/0305215X.2016.1164853.

22. Osanov M, Guest JK. Topology optimization for architected materials design. *Annual Review of Materials Research* 2016; **46**(1):211–233, doi:10.1146/annurev-matsci-070115-031826. URL https://doi.org/10.1146/annurev-matsci-070115-031826.

23. Jog C. Distributed-parameter optimization and topology design for non-linear thermoelasticity. *Computer Methods in Applied Mechanics and Engineering* 1996; **132**(1):117 – 134, doi:https://doi.org/10.1016/0045-7825(95)00990-6. URL http://www.sciencedirect.com/science/article/pii/0045782595009906.

24. Buhl T, Pedersen CBW, Sigmund O. Stiffness design of geometrically nonlinear structures using topology optimization. *Structural and Multidisciplinary Optimization* 2000; **19**(2):93–104, doi:10.1007/s001580050089. URL https://doi.org/10.1007/s001580050089.

25. Bruns TE, Tortorelli DA. Topology optimization of non-linear elastic structures and compliant mechanisms. *Computer Methods in Applied Mechanics and Engineering* 2001; **190**:3443–3459.

26. Bruns TE, Sigmund O, Tortorelli DA. Numerical methods for the topology optimization of structures that exhibit snap-through. *International Journal for Numerical Methods in Engineering* 2002; **55**(10):1215–1237, doi:10.1002/nme.544. URL https://onlinelibrary.wiley.com/doi/abs/10.1002/nme.544.

27. Bruns TE, Tortorelli DA. An element removal and reintroduction strategy for the topology optimization of structures and compliant mechanisms. *International Journal for Numerical Methods in Engineering* 2003; **57**(10):1413–1430, doi:10.1002/nme.783. URL https://onlinelibrary.wiley.com/doi/abs/10.1002/nme.783.

28. Bruns T, Sigmund O. Toward the topology design of mechanisms that exhibit snap-through behavior. *Computer Methods in Applied Mechanics and Engineering* 2004; **193**(36):3973 – 4000, doi:https://doi.org/10.1016/j.cma.2004.02.017. URL http://www.sciencedirect.com/science/article/pii/S0045782504001677.

29. Kwak J, Cho S. Topological shape optimization of geometrically nonlinear structures using level set method. *Computers & Structures* 2005; **83**(27):2257 – 2268, doi:https://doi.org/10.1016/j.compstruc.2005.03.016. URL http://www.sciencedirect.com/science/article/pii/S0045794905001963.

30. Abdi M, Ashcroft I, Wildman R. Topology optimization of geometrically nonlinear structures using an evolutionary optimization method. *Engineering Optimization* 2018; **50**(11):1850–1870, doi:10.1080/0305215X.2017.1418864. URL https://doi.org/10.1080/0305215X.2017.1418864.

31. Chen Q, Zhang X, Zhu B. A 213-line topology optimization code for geometrically nonlinear structures. *Structural and Multidisciplinary Optimization* 2019; **59**(5):1863–1879, doi:10.1007/s00158-018-2138-5. URL https://doi.org/10.1007/s00158-018-2138-5.

32. Deng H, To AC. Linear and nonlinear topology optimization design with projection-based ground structure method (p-gsm). *International Journal for Numerical Methods in Engineering* 2020; **121**(11):2437–2461, doi:10.1002/nme.6314. URL https://onlinelibrary.wiley.com/doi/abs/10.1002/nme.6314.

33. Dunning PD. On the co-rotational method for geometrically nonlinear topology optimization. *Structural and Multidisciplinary Optimization* 2020; doi:10.1007/s00158-020-02605-4. URL https://doi.org/10.1007/s00158-020-02605-4.

34. Xu B, Han Y, Zhao L. Bi-directional evolutionary topology optimization of geometrically nonlinear continuum structures with stress constraints. *Applied Mathematical Modelling* 2020; **80**:771 – 791, doi:https://doi.org/10.1016/j.apm.2019.12.009. URL http://www.sciencedirect.com/science/article/pii/S0307904X19307486.

35. Zhu B, Zhang X, Li H, Liang J, Wang R, Li H, Nishiwaki S. An 89-line code for geometrically nonlinear topology optimization written in freefem. *Structural and Multidisciplinary Optimization* 2020; doi:10.1007/s00158-020-02733-x. URL https://doi.org/10.1007/s00158-020-02733-x.

36. Yuge K, Kikuchi N. Optimization of a frame structure subjected to a plastic deformation. *Structural optimization* 1995; **10**(3-4):197–208.

37. Bendsøe MP, Díaz AR. A method for treating damage related criteria in optimal topology design of continuum structures. *Structural optimization* 1998; **16**(2-3):108–115.

38. Maute K, Schwarz S, Ramm E. Adaptive topology optimization of elastoplastic structures. *Structural optimization* 1998; **15**(2):81–91.

39. Yoon GH, Kim YY. Topology optimization of material-nonlinear continuum structures by the element connectivity parameterization. *International Journal for Numerical Methods in Engineering* 2007; **69**(10):2196–2218, doi:10.1002/nme.1843. URL https://onlinelibrary.wiley.com/doi/abs/10.1002/nme.1843.

40. Huang X, Xie Y. Topology optimization of nonlinear structures under displacement loading. *Engineering Structures* 2008; **30**(7):2057 – 2068, doi:http://dx.doi.org/10.1016/j.engstruct.2008.01.009. URL http://www.sciencedirect.com/science/article/pii/S0141029608000205.

41. Desmorat B, Desmorat R. Topology optimization in damage governed low cycle fatigue. *Comptes Rendus Mécanique* 2008; **336**(5):448 – 453, doi:http://dx.doi.org/10.1016/j.crme.2008.01.001. URL http://www.sciencedirect.com/science/article/pii/S1631072108000028.

42. Amir O, Sigmund O. Reinforcement layout design for concrete structures based on continuum damage and truss topology optimization. *Structural and Multidisciplinary Optimization* 2012; **47**(2):157–174, doi:10.1007/s00158-012-0817-1. URL http://dx.doi.org/10.1007/s00158-012-0817-1.

43. Amir O. A topology optimization procedure for reinforced concrete structures. *Computers & Structures* 2013; **114–115**:46 – 58, doi:http://dx.doi.org/10.1016/j.compstruc.2012.10.011. URL http://www.sciencedirect.com/science/article/pii/S0045794912002337.

44. Manktelow KL, Leamy MJ, Ruzzene M. Topology design and optimization of nonlinear periodic materials. *Journal of the Mechanics and Physics of Solids* 2013; **61**(12):2433 – 2453, doi:https://doi.

org/10.1016/j.jmps.2013.07.009. URL http://www.sciencedirect.com/science/article/pii/S0022509613001397.

45. James KA, Waisman H. Failure mitigation in optimal topology design using a coupled nonlinear continuum damage model. *Computer Methods in Applied Mechanics and Engineering* 2014; **268**:614 – 631, doi:http://dx.doi.org/10.1016/j.cma.2013.10.022. URL http://www.sciencedirect.com/science/article/pii/S0045782513002740.
46. Chen W, Xia L, Yang J, Huang X. Optimal microstructures of elastoplastic cellular materials under various macroscopic strains. *Mechanics of Materials* 2018; **118**:120 – 132, doi:https://doi.org/10.1016/j.mechmat.2017.10.002. URL http://www.sciencedirect.com/science/article/pii/S0167663616301430.
47. Alberdi R, Zhang G, Li L, Khandelwal K. A unified framework for nonlinear path-dependent sensitivity analysis in topology optimization. *International Journal for Numerical Methods in Engineering* 2018; **115**(1):1–56, doi:10.1002/nme.5794. URL https://onlinelibrary.wiley.com/doi/abs/10.1002/nme.5794.
48. Zhang XS, Paulino GH, Ramos AS. Multi-material topology optimization with multiple volume constraints: a general approach applied to ground structures with material nonlinearity. *Structural and Multidisciplinary Optimization* 2018; **57**(1):161–182, doi:10.1007/s00158-017-1768-3. URL https://doi.org/10.1007/s00158-017-1768-3.
49. Zhao T, Ramos Jr AS, Paulino GH. Material nonlinear topology optimization considering the von mises criterion through an asymptotic approach: Max strain energy and max load factor formulations. *International Journal for Numerical Methods in Engineering* 2020/10/20 2019; **118**(13):804–828, doi:10.1002/nme.6038. URL https://doi.org/10.1002/nme.6038.
50. Nakshatrala P, Tortorelli D, Nakshatrala K. Nonlinear structural design using multiscale topology optimization. part i: Static formulation. *Computer Methods in Applied Mechanics and Engineering* 2013; **261–262**:167 – 176, doi:http://dx.doi.org/10.1016/j.cma.2012.12.018. URL http://www.sciencedirect.com/science/article/pii/S004578251200388X.
51. Nakshatrala PB, Tortorelli DA. Nonlinear structural design using multiscale topology optimization. part ii: Transient formulation. *Computer Methods in Applied Mechanics and Engineering* 2016; **304**:605–618, doi:https://doi.org/10.1016/j.cma.2016.01.003. URL http://www.sciencedirect.com/science/article/pii/S0045782516000050.
52. Fritzen F, Xia L, Leuschner M, Breitkopf P. Topology optimization of multiscale elastoviscoplastic structures. *International Journal for Numerical Methods in Engineering* 2016; **106**(6):430–453, doi:10.1002/nme.5122. URL https://onlinelibrary.wiley.com/doi/abs/10.1002/nme.5122.
53. Xia L, Breitkopf P. Recent advances on topology optimization of multiscale nonlinear structures. *Archives of Computational Methods in Engineering* Apr 2017; **24**(2):227–249, doi:10.1007/s11831-016-9170-7. URL https://doi.org/10.1007/s11831-016-9170-7.
54. Kato J, Yachi D, Kyoya T, Terada K. Micro-macro concurrent topology optimization for nonlinear solids with a decoupling multiscale analysis. *International Journal for Numerical Methods in Engineering*

2018; **113**(8):1189–1213, doi:10.1002/nme.5571. URL https://onlinelibrary.wiley.com/doi/abs/10.1002/nme.5571.

55. Zhang G, Khandelwal K. Computational design of finite strain auxetic metamaterials via topology optimization and nonlinear homogenization. *Computer Methods in Applied Mechanics and Engineering* 2019; **356**:490 – 527, doi:https://doi.org/10.1016/j.cma.2019.07.027. URL http://www.sciencedirect.com/science/article/pii/S0045782519304232.
56. Swan CC, Arora JS. Topology design of material layout in structured composites of high stiffness and strength. *Structural optimization* 1997; **13**(1):45–59.
57. Swan CC, Kosaka I. Homogenization-based analysis and design of composites. *Computers & Structures* 1997; **64**(1–4):603–621.
58. Wang F, Sigmund O, Jensen J. Design of materials with prescribed nonlinear properties. *Journal of the Mechanics and Physics of Solids* 2014; **69**:156 – 174, doi:https://doi.org/10.1016/j.jmps.2014.05.003. URL http://www.sciencedirect.com/science/article/pii/S0022509614000866.
59. Clausen A, Wang F, Jensen JS, Sigmund O, Lewis JA. Topology optimized architectures with programmable poisson's ratio over large deformations. *Advanced Materials* 2015; **27**(37):5523–5527, doi:10.1002/adma.201502485. URL https://onlinelibrary.wiley.com/doi/abs/10.1002/adma.201502485.
60. Wang F. Systematic design of 3d auxetic lattice materials with programmable poisson's ratio for finite strains. *Journal of the Mechanics and Physics of Solids* 2018; **114**:303 – 318, doi:https://doi.org/10.1016/j.jmps.2018.01.013. URL http://www.sciencedirect.com/science/article/pii/S0022509617308438.
61. Reda H, Karathanasopoulos N, Elnady K, Ganghoffer J, Lakiss H. The role of anisotropy on the static and wave propagation characteristics of two-dimensional architectured materials under finite strains. *Materials & Design* 2018; **147**:134 – 145, doi:https://doi.org/10.1016/j.matdes.2018.03.039. URL http://www.sciencedirect.com/science/article/pii/S0264127518302181.
62. Wallin M, Tortorelli DA. Nonlinear homogenization for topology optimization. *Mechanics of Materials* 2020; **145**:103 324, doi:https://doi.org/10.1016/j.mechmat.2020.103324. URL http://www.sciencedirect.com/science/article/pii/S0167663619302418.
63. Ibrahimbegović A, Grešovnik I, Markovič D, Melnyk S, Rodič T. Shape optimization of two-phase inelastic material with microstructure. *Engineering Computations* 2005; **22**(5/6):605–645.
64. Lüdeker JK, Sigmund O, Kriegesmann B. Inverse homogenization using isogeometric shape optimization. *Computer Methods in Applied Mechanics and Engineering* 2020; **368**:113 170, doi:https://doi.org/10.1016/j.cma.2020.113170. URL http://www.sciencedirect.com/science/article/pii/S0045782520303558.
65. Wang ZP, Poh LH, Dirrenberger J, Zhu Y, Forest S. Isogeometric shape optimization of smoothed petal auxetic structures via computational periodic homogenization. *Computer Methods in Applied Mechanics and Engineering* 2017; **323**:250 – 271, doi:https://doi.org/10.1016/j.cma.2017.05.013. URL http://www.sciencedirect.com/science/article/pii/S0045782516313858.

66. Wang C, Xia S, Wang X, Qian X. Isogeometric shape optimization on triangulations. *Computer Methods in Applied Mechanics and Engineering* 2018; **331**:585 – 622, doi:https://doi.org/10.1016/j.cma.2017.11.032. URL http://www.sciencedirect.com/science/article/pii/S0045782517300543.

67. Brandyberry DR, Najafi AR, Geubelle PH. Multiscale design of three-dimensional nonlinear composites using an interface-enriched generalized finite element method. *International Journal for Numerical Methods in Engineering* 2020; **121**(12):2806–2825, doi:10.1002/nme.6333. URL https://onlinelibrary.wiley.com/doi/abs/10.1002/nme.6333.

68. Soghrati S, Geubelle P. A 3D interface-enriched generalized finite element method for weakly discontinuous problems with complex internal geometries. *Computer Methods in Applied Mechanics and Engineering* 2012; **217-220**:46–57.

69. Soghrati S, Najafi AR, Lin JH, Hughes KM, White SR, Sottos NR, Geubelle PH. Computational analysis of actively-cooled 3d woven microvascular composites using a stabilized interface-enriched generalized finite element method. *International Journal of Heat and Mass Transfer* 10 2013; **65**(0):153–164.

70. Najafi A, Soghrati S, Sottos N, White S, Geubelle P. Computational design of actively-cooled microvascular composite skin panels for hypersonic aircraft. *Proceedings of the 54th AIAA/ASME/ASCE/AHS/ASC Structures, Structural Dynamics, and Materials Conferences*, 2013.

71. Najafi AR, Safdari M, Tortorelli DA, Geubelle PH. A gradient-based shape optimization scheme using an interface-enriched generalized FEM. *Computer Methods in Applied Mechanics and Engineering* 2015; **296**:1 – 17.

72. Najafi AR, Safdari M, Tortorelli DA, Geubelle PH. Shape optimization using a nurbs-based interface-enriched generalized fem. *International Journal for Numerical Methods in Engineering* 2017; **111**(10):927–954, doi:10.1002/nme.5482. URL https://onlinelibrary.wiley.com/doi/abs/10.1002/nme.5482.

73. Zacek S, Brandyberry D, Klepacki A, Montgomery C, Shakiba M, Rossol M, Najafi A, Zhang X, Sottos N, Geubelle P, *et al.*. Transverse failure of unidirectional composites: Sensitivity to interfacial properties. *Integrated Computational Materials Engineering (ICME): Advancing Computational and Experimental Methods*, Ghosh S, Woodward C, Przybyla C (eds.). chap. 12, Springer International Publishing: Cham, 2020; 329–347, doi:10.1007/978-3-030-40562-5_12. URL https://doi.org/10.1007/978-3-030-40562-5_12.

74. Safdari M, Najafi AR, Sottos NR, Geubelle PH. A nurbs-based interface-enriched generalized finite element method for problems with complex discontinuous gradient fields. *International Journal for Numerical Methods in Engineering* 2015; **101**(12):950–964.

75. Safdari M, Najafi AR, Sottos NR, Geubelle PH. A NURBS-based generalized finite element scheme for 3d simulation of heterogeneous materials. *Journal of Computational Physics* 2016; **318**:373–390, doi:http://dx.doi.org/10.1016/j.jcp.2016.05.004. URL http://www.sciencedirect.com/science/article/pii/S0021999116301310.

76. Tan MHY, Safdari M, Najafi AR, Geubelle PH. A nurbs-based interface-enriched generalized finite element scheme for the thermal analysis and design of microvascular composites. *Computer Methods in Applied Mechanics*

and Engineering 2015; **283**(1):1382–1400.

77. Najafi A, Safdari M, Geubelle PH. Material design using a nurbs-based shape optimization. *57th AIAA/ASCE/AHS/ASC Structures, Structural Dynamics, and Materials Conference*, 2016, doi:10.2514/6.2016-1170. URL https://arc.aiaa.org/doi/abs/10.2514/6.2016-1170.

78. Najafi AR, Coppola A, Soghrati S, Sottos NR, White SR, Geubelle P. Microvascular composite skin panels for hypersonic aircraft. *55th AIAA/ASME/ASCE/AHS/ASC Structures, Structural Dynamics, and Materials Conference*, 2014, doi:10.2514/6.2014-0630. URL https://arc.aiaa.org/doi/abs/10.2514/6.2014-0630.

79. Tan MHY, Najafi AR, Pety SJ, White SR, Geubelle PH. Gradient-based design of actively-cooled microvascular composite panels. *International Journal of Heat and Mass Transfer* 2016; **103**:594 – 606, doi:https://doi.org/10.1016/j.ijheatmasstransfer.2016.07.092. URL http://www.sciencedirect.com/science/article/pii/S0017931016302666.

80. Pety SJ, Tan MHY, Najafi AR, Barnett PR, Geubelle PH, White SR. Carbon fiber composites with 2d microvascular networks for battery cooling. *International Journal of Heat and Mass Transfer* 2017; **115**:513 – 522, doi:https://doi.org/10.1016/j.ijheatmasstransfer.2017.07.047. URL http://www.sciencedirect.com/science/article/pii/S0017931017311146.

81. Tan MHY, Najafi AR, Pety SJ, White SR, Geubelle PH. Multi-objective design of microvascular panels for battery cooling applications. *Applied Thermal Engineering* 2018; **135**:145 – 157, doi:https://doi.org/10.1016/j.applthermaleng.2018.02.028. URL http://www.sciencedirect.com/science/article/pii/S1359431117357332.

82. Pety SJ, Tan MHY, Najafi AR, Gendusa AC, Barnett PR, Geubelle PH, White SR. Design of redundant microvascular cooling networks for blockage tolerance. *Applied Thermal Engineering* 2018; **131**:965 – 976, doi:https://doi.org/10.1016/j.applthermaleng.2017.10.094. URL http://www.sciencedirect.com/science/article/pii/S1359431117328144.

83. Pejman R, Aboubakr SH, Martin WH, Devi U, Tan MHY, Patrick JF, Najafi AR. Gradient-based hybrid topology/shape optimization of bioinspired microvascular composites. *International Journal of Heat and Mass Transfer* 2019; **144**:118 606, doi:https://doi.org/10.1016/j.ijheatmasstransfer.2019.118606. URL http://www.sciencedirect.com/science/article/pii/S0017931019316849.

84. Pejman R, Maghami E, Najafi AR. How to design a blockage-tolerant cooling network? *Applied Thermal Engineering* 2020; **181**:115 916, doi:https://doi.org/10.1016/j.applthermaleng.2020.115916. URL http://www.sciencedirect.com/science/article/pii/S1359431120333986.

85. Pejman R, Keshavarzzadeh V, Najafi AR. Hybrid topology/shape optimization under uncertainty for actively-cooled nature-inspired microvascular composites. *Computer Methods in Applied Mechanics and Engineering* 2021; **375**:113 624, doi:https://doi.org/10.1016/j.cma.2020.113624. URL http://www.sciencedirect.com/science/article/pii/S0045782520308094.

86. Najafi AR. Multiscale design of nonlinear materials using a shape optimization scheme based on an interface-enriched gfem. PhD Thesis, University of Illinois at Urbana-Champaign 2016.
87. Piegl L, Tiller W. *The NURBS Book*. 2nd edn. edn., U.S. Government Printing Office, Springer: New York, 1997.
88. Benssousan A, Lions J, Papanicoulau G. *Asymptotic analysis for periodic structures*. North-Holland, Amsterdam, 1978.
89. Sanchez-Palencia E, Zaoui A ((eds.)). *Homogenization techniques for composite media*, *Lecture Notes in Physics, Berlin Springer Verlag*, vol. 272, 1987.
90. Guedes J, Kikuchi N. Preprocessing and postprocessing for materials based on the homogenization method with adaptive finite element methods. *Computer Methods in Applied Mechanics and Engineering* 10 1990; **83**(2):143–198.
91. Simo JC, Ju JW. Strain- and stress-based continuum damage models—I. formulation. *International Journal of Solids and Structures* 1987; **23**(7):821–840.
92. Simo JC, Ju JW. Strain- and stress-based continuum damage models—I. computational aspects. *International Journal of Solids and Structures* 1987; **23**(7):841–869.
93. Matous K, Kulkarni MG, Geubelle PH. Multiscale cohesive failure modeling of heterogeneous adhesives. *Journal of the Mechanics and Physics of Solids* Apr 2008; **56**(4):1511–1533.
94. Matouš K, Kulkarni MG, Geubelle PH. Multiscale cohesive failure modeling of heterogeneous adhesives. *Journal of the Mechanics and Physics of Solids* 4 2008; **56**(4):1511–1533.
95. Michaleris P, Tortorelli DA, Vidal CA. Tangent operators and design sensitivity formulations for transient non-linear coupled problems with applications to elastoplasticity. *International Journal for Numerical Methods in Engineering* 1994; **37**(14):2471–2499, doi:10.1002/nme.1620371408. URL http://dx.doi.org/10.1002/nme.1620371408.
96. Kulkarni DV, Tortorelli DA, Wallin M. A newton–schur alternative to the consistent tangent approach in computational plasticity. *Computer Methods in Applied Mechanics and Engineering* 2007; **196**(7):1169 – 1177, doi:https://doi.org/10.1016/j.cma.2006.06.013. URL http://www.sciencedirect.com/science/article/pii/S0045782506002180.
97. Simo J, Taylor R. Consistent tangent operators for rate-independent elastoplasticity. *Computer Methods in Applied Mechanics and Engineering* 1985; **48**(1):101 – 118, doi:https://doi.org/10.1016/0045-7825(85)90070-2. URL http://www.sciencedirect.com/science/article/pii/0045782585900702.
98. Rogers DF. *An introduction to NURBS: with historical perspective*. Morgan Kaufmann Publishers: San Francisco, CA, USA, 2001.
99. Hughes T, Cottrell J, Bazilevs Y. Isogeometric analysis: Cad, finite elements, nurbs, exact geometry and mesh refinement. *Computer Methods in Applied Mechanics and Engineering* 2005; **194**(39–41):4135 – 4195.
100. Dayar T. *Analyzing Markov chains using Kronecker products: theory and applications*. Springer Science & Business Media, 2012.